Experimental and Theoretical Investigation of SiC/SiC Composites under Multiaxial Loading

A DISSERTATION

SUBMITTED TO THE FACULTY OF THE GRADUATE SCHOOL

OF THE UNIVERSITY OF MINNESOTA

BY

Chen Hu

IN PARTIAL FULFILLMENT OF THE REQUIREMENTS

FOR THE DEGREE OF

DOCTOR OF PHILOSOPHY

Advisors:

Joseph F. Labuz

Jia-Liang Le

September, 2023

Acknowledgements

I wish to dedicate this chapter to acknowledging and expressing gratitude to everyone who has supported me throughout my past nine years in the United States.

First and foremost, I extend my profound appreciation to my supervisors, Professor Joseph F. Labuz and Professor Jia-Liang Le. My academic journey with Professor Labuz commenced in his Soil Mechanics class, eventually blossoming as I transitioned into his Ph.D. student. Throughout this time, he has generously guided me with a nurturing spirit, encouraging me to carve my own path in research. At the beginning of the SiC/SiC project, we were confronted with the substantial challenge of designing a testing apparatus that could introduce high pressure to load the specimen to its ultimate failure. The initial stages were characterized by a relentless cycle of design, testing, failure, analysis, and iteration. I vividly recall a period when Professor Labuz, Mugurel, and I were engulfed in a whirlpool of fatigue due to the repetitive process. On one occasion, our differing perspectives led to a mild disagreement concerning the design. Despite the momentary discord, Professor Labuz exhibited remarkable grace the following day, presenting me with a box of homemade chocolates from his wife. This heartfelt gesture, perhaps accompanied by a stroke of luck, seemed to inaugurate a turning

point, steering our project toward the successful fulfillment of our requirements. My upbringing in China immersed me in the philosophies of Confucianism, encapsulated in the principle of "benevolence and love towards others". Although I was familiar with this theory, embodying it remained a mystery until Professor Labuz embodied it, enlightening me through his actions and demonstrating the practical application of this philosophy in nurturing the human-to-human relationship.

In my formative years as a young individual, I often found myself grappling with the uncertainty of the path I wished to tread in the future. It was during this period of introspection and self-doubt that Professor Jia-Liang Le emerged as a beacon of guidance and clarity. His profound understanding of theoretical fracture mechanics and reliability analysis not only enriched my knowledge but also reshaped my perspective toward research. Through his enlightening lecture on Fracture and Scaling, he ushered me into a realm where I could appreciate the intricate beauty of mechanisms that govern our world. This experience profoundly influenced my outlook, encouraging me to delve deeper into the subject matter, rather than merely scratching the surface. His teachings instilled in me the belief that dedicating time to ponder profoundly on theorems is not in vain but a vital step towards genuine comprehension and mastery. Furthermore, Professor Le emphasized the significance of giving one's utmost effort in every endeavor, a lesson encapsulated in his words: "No matter what to do, you should do your best." This sage advice resonated deeply with me, particularly during moments when I found myself veering towards the path of least resistance, seeking easier or more fancy routes. Under his mentorship, I learned to nurture a strong determination, steering clear of transient attractions and focusing on the foundational aspects of

research, a discipline that requires one's unreserved commitment and passion.

More than a mere occupation aimed at securing a foothold in the world or achieving fleeting success, research, for me, has transformed into a cherished hobby that promises joy and intellectual fulfillment. It stands as a pursuit where one can attain ultimate mental success and happiness, elements that I now regard as lifelong objectives worthy of pursuit and dedication.

I wish to express my heartfelt gratitude to my fiancée, Dr. Manyan Huang. Our journey together began in high school, where she was my quiet and reserved classmate, seated just ahead of me. Our paths then diverged, only to miraculously converge again as we individually chose to further our studies in the United States. It astounds me to think of the tremendous growth and adventures that transformed that shy young girl into a remarkable woman who now stands beside me, ready to share a lifetime of joy and companionship. I acknowledge that my temperament can sometimes be hasty and stubborn, with a tendency to be careless with my choice of words. She, being the person who engages with me most on a daily basis, gracefully navigates through these traits of mine. Her unyielding patience has been a sanctuary for my spirit, while her distinctive love has exponentially amplified the value and purpose I find in life.

During my Ph.D. journey, Dr. Tianhao Yan and Dr. Xiaoran Wang have been two of my closest friends. Their unwavering reliability and exemplary character have been a source of constant inspiration. Whether it was engaging in thought-provoking research discussions, pondering future career paths over after-dinner conversations, or hiking together in Minnesota's state parks, they brought

vibrancy to my Ph.D. experience. As they continue to chase their research aspirations, I fervently hope for their success. On the technical front, Mr. Mugurel has been my go-to for any experimental queries. Together, we designed the multiaxial testing apparatus. His unparalleled kindness and patience have benefitted all the Ph.D. students on the third floor of the Civil Engineering building, making him an indispensable figure across all our labs.

Throughout my enriching journey in the CEGE department, I have acquired a wealth of knowledge and developed a dedicated approach to research. My time here has also cultivated my teaching and mentoring abilities, instilling in me the values of kindness and compassion. I am profoundly grateful to all the professors who illuminated my path with their meticulously crafted lectures, guiding me through the expansive corridors of knowledge.

I echo my fiancée's heartfelt wish for a life filled with happiness and good health, a sentiment I extend to everyone who has touched my life over the past nine years. To my professors, parents, friends, colleagues, and even those I have yet to meet, I sincerely wish you all a lifetime of happiness and enduring health.

Dedication

For the admirers of "The starry heavens above me and the moral law within me."

Abstract

Owing to its excellent mechanical properties and stability under high temperature and neutron irradiation conditions, SiC/SiC composites have emerged as promising materials for light water reactors (LWRs) in the development of accident-tolerant fuel (ATF) systems. Structural integrity and retention of hermeticity are two crucial requirements for SiC/SiC claddings during normal operations, and both of them are closely related to the material's proportional limit stress (PLS). Understanding the behavior of SiC/SiC composites under multiaxial stress states and developing a probabilistic approach for evaluating the structural vulnerability is of paramount importance for reliability-based analysis and design of SiC/SiC composite claddings. So far, there has been very limited effort towards experimental and analytical investigations of probabilistic failure of SiC/SiC claddings. This critical knowledge gap motivates the research presented in this dissertation.

A probabilistic failure criterion is developed for SiC/SiC composites under multiaxial loading, and this criterion is incorporated into the reliability analysis of the structural integrity of SiC/SiC fuel cladding. The research consists of two parts: 1) experimental investigation of multiaxial failure behavior of SiC/SiC composites, and 2) theoretical modeling of time-dependent probabilistic failure of SiC/SiC cladding. In the experimental investigation, the PLS is determined by examining stress-strain response and acoustic emission measurements. The theoretical framework is derived by combining the finite weakest-link statistical model

and the subcritical damage growth model. This theoretical model captures the time-dependent failure mechanism of the material, which has a major consequence in predicting the lifetime distribution of the cladding. Meanwhile, the model also predicts that the failure statistics of the cladding depend strongly on the cladding length.

The results of the multiaxial experiments reveal the level of statistical variation of the PLS of SiC/SiC materials under different stress states. The theoretical model provides a robust analytical tool for extrapolation of small-scale laboratory test results to the behavior of full-scale claddings. These findings lay down a scientific foundation for the development of the reliability-based design of SiC/SiC fuel claddings, which will play an essential role in improving the structural safety and integrity of LWRs.

Contents

Acknowledgements **i**

Dedication **v**

Abstract **vi**

Contents **viii**

List of Tables **xi**

List of Figures **xii**

1 Introduction **1**

2 Overview of SiC materials **7**

2.1 Silicon carbide (SiC) 7

2.2 SiC-based materials 9

2.3 SiC/SiC composites 11

2.3.1 SiC/SiC composites in nuclear application 12

2.4 Material used in this project 13

3 Multiaxial Experiments for SiC/SiC composites **17**

3.1 Multiaxial testing system 17

3.2 Strain measurement and AE system 20

3.3 Loading protocol 23

3.4 Determination of PLS 24

3.5 Mean strength and damage pattern 28

3.6 Multiaxial failure surface 31

3.7 Probabilistic model of multiaxial PLS 34

4 Time-dependent Probabilistic Failure Model **40**

4.1 Stress-based failure criterion 40

4.2 Extension to time-dependent failure behavior 41

5 Finite Weakest Link Model for Design Extrapolation **45**

5.1 Background on weakest-link model 46

5.2 Weibull theory 48

5.3 Scaling of Weibull theory and pure statistical size effect 50

5.4 Finite weakest-link model for SiC/SiC nuclear claddings 54

6 Reliability Analysis of SiC/SiC Claddings **58**

6.1 Description of analysis 58

6.2 Time evolution of failure probability 62

6.3 Spatial distribution of failure probability 65

6.4 Failure probability of entire cladding and the effect of damage growth rate 67

6.5 Effect of the cladding length to failure probability 70

7 Conclusion and Recommendations **73**

7.1 Conclusions 73

7.2 Recommendations 75

References **77**

Appendix A. Strength Parameters for Individual Tests **85**

List of Tables

2.1 Mechanical properties of 2D CVI SiC/SiC composites under different temperatures [1]. 13

2.2 Mechanical properties of CVI SiC/SiC composites nonirradiated and irradiated under LWR-relevant temperature and dose conditions [2]. 14

3.1 Mean and standard deviation (data in parenthesis) of the AE-defined PLS, strain-defined PLS, and UTS for five load paths. . . 29

3.2 Model parameters for fitting histogram of f_{tz}, $f_{t\theta}$, and f_b. 37

A.1 Strength parameters for uniaxial tension tests. 85

A.2 Strength parameters for hoop tension tests. 86

A.3 Strength parameters for biaxial tension tests. 86

A.4 Strength parameters for loading path $\sigma_{zz}/\sigma_{\theta\theta} = 2$. 87

A.5 Strength parameters for loading path $\sigma_{zz}/\sigma_{\theta\theta} = 0.5$. 87

List of Figures

2.1 Specimen prepared (left) and similar specimen observed by optical microscopy and scanning electron microscopy (right) [3]. 16

3.1 Schematic of loading configuration of SiC/SiC cladding. 19

3.2 Membrane and loading apparatus. 21

3.3 Alignment tool. 21

3.4 Multiaxial testing and data acquisition system. 22

3.5 Stress-strain responses of five loading paths: (a) uniaxial tension test (with ASTM offset method), (b) hoop tension test, (c) $\sigma_{zz}/\sigma_{\theta\theta} = 2$, (d) biaxial tension test, and (e) $\sigma_{zz}/\sigma_{\theta\theta} = 0.5$. 25

3.6 (a) Comparison of cumulative RMS and AE count curve, and (b) cumulative AE count curve and its slope from a SiC/SiC multiaxial test. 27

3.7 Specimen failure patterns for (a) uniaxial tension test (b) biaxial tension test, and (c) hoop tension test. 31

3.8 PLS failure surface of SiC/SiC composites. 33

3.9 Probability distributions of strength in different loading paths: (a) unaxial tension test, (b) hoop tension test, (c) $\sigma_{zz}/\sigma_{\theta\theta} = 2$, (d) biaxial tension test, and (e) $\sigma_{zz}/\sigma_{\theta\theta} = 0.5$. 35
3.10 Gauss-Weibull fitting of measured histograms of (a)f_{tz}, (b)$f_{t\theta}$, and (c)f_b. 37
3.11 Measured and predicted probability distributions of PLS for (a) $\sigma_{zz}/\sigma_{\theta\theta} = 2$, and (b) $\sigma_{zz}/\sigma_{\theta\theta} = 0.5$ 39
4.1 Loading protocols: a) reference ramped loading, and b) general loading history. 42
5.1 Weakest-link model of strength statistics. 47
5.2 Calculation of mean structural strength. 52
6.1 Time histories of axial and hoop stresses of the inner layer of the cladding at its mid-height [4]. 60
6.2 Spatial distribution of axial and hoop stresses at 2 years of service along the height of the cladding [4]. 61
6.3 Failure probability of the inner layer of the cladding calculated using the stresses at its mid-height. 64
6.4 Time evolution of contribution of applied stress on the damage growth at the mid-height of the inner layer. 65
6.5 Spatial distribution of failure probability of one column of inner-layer elements over a period of 24 months. 66
6.6 Lifetime distribution of the entire cladding; for a tolerable failure risk of 10^{-6}, the cladding should be inspected after $t_f = 16.6$ months of service. 67

6.7 (a) Lifetime distributions of cladding calculated by using different n values and a time-independent model, and (b) the corresponding service lifetimes corresponding to $P_f = 10^{-6}$. 70
6.8 Length effect on the failure probability of the cladding. 71
6.9 Length effect on the service lifetime of the cladding corresponding to $P_f = 10^{-6}$. 72

Chapter 1

Introduction

The 2011 Fukushima Daiichi nuclear power plant accident has stimulated the active development of accident-tolerant fuels (ATFs) and accident-tolerant cores [5]. In recent years, silicon carbide (SiC) fiber-reinforced SiC matrix (SiC/SiC) composites have attracted increasing attention as an alternative material for fuel cladding in light water reactors (LWRs) [6]. Extensive experimental research showed that the SiC/SiC composites can retain excellent mechanical properties under high temperature and neutron irradiation conditions. Compared to traditional Zirconium alloy cladding and core, which would produce explosive hydrogen in a water vapor environment, SiC/SiC composites exhibit general chemical inertness at very high temperatures [7]. Moreover, they are also stable under high-dose neutron radiation [6]. Owing to these attractive features, SiC/SiC composites are considered favorable for providing passive safety for LWRs in beyond-design-basis severe accident scenarios [5].

For LWR fuel claddings, SiC/SiC composites are fabricated in the form of long tubes. Considerable efforts have been devoted towards experimental investigations

of SiC/SiC composite tubes under different loading scenarios including uniaxial tension, hoop tension, and multiaxial loading [8, 3, 9, 10, 11]. It is generally observed that the specimen would exhibit a linear elastic behavior up to a stress level referred to as the proportional limit stress (PLS). Upon reaching the PLS, the matrix material experiences notable damage and the specimen shows a reduction of stiffness. As damage accumulates in the matrix, the fibers start to take more loading. This eventually leads to localized fiber breakage, and the specimen attains its ultimate tensile strength (UTS). For the purpose of cladding design, the PLS and UTS are two critical metrics. It is considered that the PLS indicates the stress level at which damage poses the risk of a gas release, whereas the UTS corresponds to the scenario in which the structure loses its load capacity. One important observation made from a recent inter-laboratory round-robin study is that the PLS and UTS of SiC/SiC composites exhibit a considerable level of variability. The measured coefficients of variation of PLS and UTS are 9.7% and 12.5%, respectively [3].

Despite the aforementioned experimental efforts, only one study has reported the failure surface of SiC/SiC composites under multiaxial loading [8]. Procedures for uniaxial and hoop tensile tests for SiC/SiC composites have been well established (ASTM C1773 and ASTM C1819). So far, limited efforts have been devoted to multiaxial loading. Furthermore, for hoop tensile tests the current test method relies on elastomeric inserts [11]. However, friction between the elastomeric insert and the internal surface of the specimen may cause unpredictable shear stresses, which affect the measurement of material strength parameters. Therefore, a more robust and reliable testing system is needed.

The statistical nature of PLS and UTS of SiC/SiC composites can be attributed to the heterogeneity of the material. In the manufacturing process, the SiC matrix is deposited from gaseous reactants onto a heated substrate of fibrous preforms of SiC [1]. This process, called chemical vapor infiltration (CVI), inevitably introduces internal pores in the matrix. It was reported that the porosity of SiC/SiC composites is in the range of 8-17% [12, 8]. The computed X-ray tomography showed that the large pores between fiber tows are crucial to damage development compared to small pores [13]. The size and location of these internal pores are affected by fiber architecture and kinetics of deposition. The uncertainty in the manufacturing process leads to statistical variation in both local stress field and material resistance and consequently the macroscopically observed variability in PLS and UTS.

The observed variability of PLS and UTS has important implications for the design of SiC/SiC composite claddings. It is widely acknowledged that engineering structures must be designed against an acceptable risk level. In the current design approach, an empirical reduction factor is applied to the PLS to account for its uncertainty [14]. This concept is similar to safety factors used in the design of concrete and steel structures. The safety factors allow us to perform reliability-based structural design through deterministic analysis. The essential step is to relate the safety factors to the failure risk of the structure [15, 16, 17]. Evidently, this relation must be derived from a probabilistic model of structural failure.

In recent years, considerable attention has been directed towards the investigation of the failure statistics of SiC/SiC composites. Previous studies have largely used the two-parameter Weibull distribution for the probability distributions of

PLS and UTS [3, 18, 19]. The Weibull distribution belongs to the class of extreme value statistics [20, 21, 22, 17], which indicates that the failure statistics of the structure can be represented by an infinite weakest-link model. Physically, it implies that a damage localization mechanism exists and that the structure must be much larger than the size of the damage zone. A series of recent studies discussed the applicability of the Weibull distribution for strength statistics of structures made of quasi-brittle materials, such as composites and ceramics, which feature a strain softening behavior and damage localization mechanism [23, 24, 25, 17]. It was shown that, for most quasi-brittle structures, the structure size is not sufficiently large to guarantee the validity of the Weibull distribution. The same issue also applies to SiC/SiC composite tubes. While the full-length cladding is 4m long, the laboratory test specimen is typically less than 100 mm, which is not significantly larger than the size of the damage zone. Therefore, the classical Weibull model cannot be used to extrapolate the laboratory test result to full-scale cladding design.

In addition to the inapplicability of the Weibull distribution for design extrapolation, probabilistic modeling of SiC/SiC composite tubes is further complicated by the time evolution of the internal stress state. A thermomechanical analysis was recently performed to investigate the stress history of the SiC/SiC cladding over its service lifetime [26, 4]. It was shown that the cladding experiences a complicated stress history along axial and hoop directions in LWRs. To model the lifetime of the cladding, it is crucial to take into account the damage accumulation mechanism. The failure probability of the entire structure at the present time depends not only on the current stress state but also on the prior loading

history. So far, such a time-dependent behavior has not been investigated.

In this study, we develop a probabilistic failure criterion for SiC/SiC composites under multiaxial loading and incorporate the criterion into the reliability analysis of the structural integrity of SiC/SiC fuel cladding. The research consists of two parts: 1) experimental investigation of multiaxial failure behavior of SiC/SiC composites, and 2) theoretical modeling of time-dependent probabilistic failure of SiC/SiC cladding. In the experimental investigation, the PLS is determined through the examination of stress-strain response and the acoustic emission measurement. The theoretical framework is derived by combining the finite weakest-link statistical model and the subcritical damage growth model. This theoretical model captures the time-dependent failure mechanism of the material, which has a major consequence in predicting the lifetime distribution of the cladding. Meanwhile, the model also predicts that the failure statistics of the cladding depend strongly on the cladding length. The results of the multiaxial experiments reveal the level of statistical variation of the PLS of SiC/SiC materials under different stress states. The theoretical model provides a robust analytical tool for extrapolation of small-scale laboratory test results to the behavior of full-scale claddings. These findings lay down a scientific foundation for the development of the reliability-based design of SiC/SiC fuel claddings, which will play an essential role in improving the structural safety and integrity of LWRs.

Based on the aforementioned content, this dissertation includes the following chapters:

- Chapter 2 briefly presents the background of SiC, SiC-based materials, and SiC/SiC composites.

- Chapter 3 describes the multiaxial experiments that were conducted.
- Chapter 4 formulates the time-dependent probabilistic model that was developed.
- Chapter 5 explains the finite weakest link model for design extrapolation.
- Chapter 6 illustrates the present model's effect on the reliability of SiC/SiC claddings
- Chapter 7 summarizes the main conclusions of this study.

Chapter 2

Overview of SiC materials

This dissertation examines silicon carbide (SiC) fiber-reinforced SiC matrix (SiC/SiC) composites, which are utilized as promising materials for nuclear plant claddings. However, to gain a thorough understanding of the evolution and the rise of SiC/SiC composites in contemporary nuclear applications, this chapter offers an in-depth overview of SiC ceramic materials. The discussion encompasses pure SiC, SiC-based materials, and SiC-SiC matrix composites, culminating in the specific SiC/SiC composites used in this project. We will briefly delve into their historical development, material properties, manufacturing processes, and applications.

2.1 Silicon carbide (SiC)

Silicon carbide (SiC), also known as carborundum, is a hard chemical compound containing silicon and carbon. This material has a very high decomposition temperature (2830 °C) and attractive oxidation resistance. Natural SiC was first discovered in the Canyon Diablo meteorite in Arizona by Moissan in 1893 [27] and

named moissanite. However, given the rarity of natural moissanite, the majority of SiC available today is manufactured synthetically. The industrial production of SiC is attributed to the efforts of Edward Goodrich Acheson in 1891, where he attempted to produce artificial diamonds through the reaction of natural clay with carbon [28]. He called the blue crystals that formed "carborundum", believing it to be a new compound of carbon and aluminum, similar to corundum. Acheson patented the method for making silicon carbide powder on February 28, 1893 [28]. Today the Acheson process is still dominantly used for producing SiC abrasive [29].

In the Acheson furnace, the purity of the resulting material can vary significantly. Recognizing this, Lely introduced a method to develop usable single-crystal SiC material, a method now known as the Lely process. In this approach, SiC undergoes sublimation within a graphite furnace and is epitaxially regrown on a central graphite rod [30]. Nevertheless, the mass production of high-quality single-crystal SiC material only became feasible in 1978, thanks to the innovations presented by Tairov and Tsvetkov, who pioneered "seeded" sublimation and growth techniques [31]. This development fundamentally marked the commencement of the modern era of SiC wafer technology.

In addition to single-crystal materials, various manufacturing techniques have been developed to create SiC ceramics that approach theoretical density. In the middle of the 20th century, Kendall and Yeo documented the synthesis of phase-pure SiC in a bulk form through the use of the chemical vapor deposition (CVD) process [32]. This method, along with contemporary wafer technologies for SiC production, currently stands as the sole approach capable of yielding fully dense,

phase-pure, and stoichiometric SiC materials, positioning them as a premium segment within the SiC market. Moreover, the production of CVD SiC can be adapted based on the processing conditions and specific application needs, such as heightened resistance to oxidation. Depending on these factors, CVD SiC can manifest as either phase-pure but highly faulted β-SiC or in a Si-rich state.

2.2 SiC-based materials

Alternatively, SiC-based materials represent materials in which SiC acts as the chief component, often amalgamated with other substances to augment specific characteristics. Unlike almost pure SiC, these materials might incorporate surplus amounts of elements such as Al, Si, B, and C. The creation of these materials is subject to the manufacturing techniques employed, with some yielding stoichiometric SiC substances and others generating SiC-based materials.

Furthermore, the efficacy of SiC-based materials is significantly dictated by the composition and spatial distribution of the present non-SiC phase(s). Specifically, the presence of these phases, either as a continuous grain boundary layer or as a pervasive structure within the ceramic, can be a pivotal factor in determining the overall performance. Generally, in the context of bulk ceramics production, only the commercial single-crystal and CVD SiC procedures are capable of fabricating phase-pure and completely dense SiC. In contrast, the remaining ceramic production techniques cultivate SiC-based materials exhibiting varying levels of density and purity, characterized by a multitude of multi-phase microstructures. A comprehensive delineation of the distinctions between monolithic SiC and SiC-based ceramics is elucidated in Table 1 in [29].

SiC and SiC-based materials have found extensive applications spanning everyday items to high-end products. These materials are pivotal in a host of thermal and abrasive applications, marking their largest segment of utilization. Interestingly, the foundation of SiC's application in the electrical sphere dates back to 1907 when H.J. Round penned a letter to the Electric World magazine, illustrating an experiment where a voltage applied to a SiC crystal resulted in the emission of yellow, green, and orange lights at the cathode, a phenomenon which later laid the groundwork for the development and commercialization of LEDs [33].

In the automotive sector, the integration of silicon within carbon-carbon composites has revolutionized brake disk technology, giving birth to high-performance "ceramic" brake disks capable of enduring extreme temperature variations. Presently, the electronic industry also capitalizes on SiC's exceptional properties by incorporating it in an extensive range of devices like metal-oxide-semiconductor field-effect transistors (MOSFETs), which are prominent in high-power switching applications, and Schottky barrier diodes (SBDs) [34].

Moreover, SiC's influence extends to specialized sectors such as aerospace. In this sector, the material's robust interest is mirrored by its widespread use in high-performance military and commercial jet engines, inclusive of its integration in the General Electric Advent engine fan blade and shroud situated in the hot section of the F136 fighter and LEAP engines, gracing renowned aircraft such as the Boeing 737 Max and Airbus A320/321Neo [35, 36, 37].

2.3 SiC/SiC composites

SiC fiber-reinforced SiC matrix (SiC/SiC) composites represent a subset of SiC-based materials and fall under the broader category of ceramic matrix composites (CMC) [38]. These composites can also be referred to as SiC–SiC matrix composites or SiC_f-SiC_m composites. Their origin can be traced back to the 1970s when they were developed from polymer precursors like polycarbosilane (PCS). Yajima's work on using PCS for SiC-based fibers laid the foundation for the commercialization of continuous fiber ceramic matrix composites [39, 40, 34]. In subsequent years, extensive research has been dedicated to identifying alternative polymers to PCS, aiming to enhance the overall quality, production yield, and industrial feasibility of SiC-based ceramics [41].

The emergence of the polymer-to-continuous-fiber technique paved the way for textile-based methods in composite manufacturing. A typical manufacturing sequence for these composites starts with determining the composite architecture, often termed fiber architecture. Subsequent steps involve weaving fibers to produce preforms—this weaving could be 2D, 3D, or even more complex, incorporating techniques such as braiding and filament winding—before matrix formation. A standout quality of these ceramic matrix composites is their damage tolerance; many such materials can maintain sufficient structural integrity despite significant mechanical damage. The interfaces between fibers and matrices are vital for this resilience. They are responsible for tasks like load transfer, matrix crack deflection through debonding, and energy dissipation via frictional sliding. This vital interplay is supported by the interphase, typically composed of carbon or boron nitride, especially in the context of SiC-based composites [29, 42, 43].

Owing to a myriad of advantages such as intrinsic high-temperature resilience, crafted damage tolerance paired with remarkable specific strength, and the capability for near-net shaping, the development of SiC-fiber composite technologies has been vigorously pursued. These technologies find promising applications in areas like ground-based gas turbines, both military and commercial aerospace engines, and ballistic armor.

2.3.1 SiC/SiC composites in nuclear application

While SiC/SiC composites boast intrinsic high-temperature capabilities and engineered damage tolerance, their radiation stability is a critical factor to consider, particularly in nuclear applications. Earlier studies indicated that the first and second-generation SiC fibers were susceptible to radiation instability, as substantiated by multiple independent research efforts [44, 45, 46, 47, 48].

Nonetheless, advancements have been made with the commercial introduction of the third generation of fibers. The Hi-Nicalon^{TM} Type-S, a prominent Generation III product, undergoes a two-stage pyrolysis process involving hydrogen and argon after electron beam curing, resulting in heightened crystallinity with minimized oxygen and free carbon content. Similarly, the Tyranno-SA3, another widely studied Generation III SiC fiber, attains an even greater degree of crystallinity through a high-temperature, aluminum-assisted sintering process [29, 49].

When these near-stoichiometric SiC$\sim$1 fibers are amalgamated with a chemical vapor infiltrated (CVI) SiC matrix and a pyrocarbon (PyC) interphase [50, 51],

the resulting composites demonstrate impressive radiation immunity and high-temperature resistance [52, 53, 54]. A detailed overview of the mechanical properties of these CVI SiC/SiC composites, under conditions of neutron irradiation and high temperatures, can be found in Table 2.1 and 2.2.

Property	23°C	1000°C	1400°C
Young's Modulus [GPa]	230	200	170
Tensile Strength [MPa]	200	200	150
Flexural Strength [MPa]	300	400	280
In-plane Compressive Strength [MPa]	580	480	300
Fracture Toughness [MPa*$m^{1/2}$]	30	30	30

Table 2.1: Mechanical properties of 2D CVI SiC/SiC composites under different temperatures [1].

Given their superior attributes, SiC/SiC composites are being explored as potential substitutes for Zircaloy cladding in light water reactors. This consideration stems partly from the fact that Zircaloy undergoes hydrogen embrittlement, a byproduct of its corrosive interaction with water, which diminishes its fracture toughness, particularly with a rising proportion of radial hydrides. This degradation escalates substantially as temperatures increase, adversely affecting the material [55]. Contrarily, SiC/SiC cladding maintains its strength properties even at heightened temperatures, avoiding the mechanical deterioration that is characteristic of Zircaloy [56, 57].

2.4 Material used in this project

The experiments used SiC/SiC tube specimens. These specimens were composed of Hi-Nicalon Type S fibers, a pyrocarbon (PyC) interlayer, and a high-purity SiC

Material (Interphase type)	Irradiation conditions	Test method	Young's modulus [GPa]	PLS [MPa]	UTS [MPa]
HNS CVI SiC/SiC plate (PyC_{20nm}/SiC_{100nm})	Nonirradiated	Cyclic tensile	232 (25)	97 (24)	284 (19)
	570°C/2.2 dpa		226 (27)	126 (12)	224 (13)
			197 (19)	116 (12)	171 (38)
HNS CVI SiC/SiC plate (PyC_{20nm}/SiC_{100nm})	Nonirradiated	Four point flexural	Not available	375.0 (50.9)	469.9 (70.1)
	300°C/3.4 dpa		Not available	332.4 (4.5)	420.4 (29.8)
HNS CVI SiC/SiC plate (PyC 50 –160 nm)	Nonirradiated	Dynamic four point flexural	255 (6)	216 (8)	412 (35)
	280–340°C/ 2.0 dpa		236 (24)	260 (28)	509 (49)
	230–280°C/ 11.8 dpa		210 (13)	226 (45)	486 (72)
SA3 CVI SiC/SiC plate (PyC 200–350 nm)	Nonirradiated	Dynamic four point flexural	241 (11)	331 (91)	493 (59)
	280–340°C/ 2.0 dpa		241 (22)	300 (40)	513 (87)
	230–280°C/ 11.8 dpa		220 (7)	344 (85)	482 (74)

Table 2.2: Mechanical properties of CVI SiC/SiC composites nonirradiated and irradiated under LWR-relevant temperature and dose conditions [2].

matrix. The fibers are near stoichiometric, display considerable stability under neutron irradiation, demonstrate limited irradiation creep, and are capable of sustaining thermal creep strength up to 1400°C [58, 59]. The tensile strength and Young's modulus of these fibers are on the order of 2 GPa and 400 GPa, respectively [60, 61]. The architecture of the fibers has a major influence on the properties of the composites, including anisotropy. For the materials used in this study, fiber preforms were constructed using a triaxial braiding technique,

enabling the fabric to adapt to intricate shapes and maintain balance on both sides. Two fiber tow bundles were arranged in a ± 55° orientation, with the other fiber bundles set at a 0° direction for axial reinforcement. A PyC monolayer of less than 250 nm was infiltrated to establish an interphase coating between the fiber and matrix within the SiC/SiC specimens. This interphase coating, which is weaker and more compliant than both the fiber and matrix, diverts cracks that propagate through the matrix, prevents fiber damage, facilitates fiber debonding and sliding, and bridges matrix cracks. These mechanisms lead to a pseudo-ductile behavior of SiC/SiC composites. After the PyC layer was formed, a SiC matrix was deposited onto a heated substrate of fibrous SiC preforms using gaseous reactants [1]. This CVI process is recognized as the most reliable method for producing a high-purity, crystalline SiC matrix, a prerequisite for ensuring optimal irradiation resistance in nuclear applications [6]. Further details on fiber development and the CVI processing route of this type of SiC/SiC composites can be found in [62, 63].

Each original tube specimen supplied by General Atomics (GA) of the length 300 ± 1 mm was cut into four specimens of 73 ± 0.3 mm by using a diamond saw. The cut edges were further polished to ensure a smooth surface devoid of any pulled-out fibers. The nominal outer diameter and inner diameter of the specimens, as determined by caliper measurements, were reported to be 9.5 ± 0.2 mm and 7.8 ± 0.2 mm, respectively. However, owing to the woven structure and intrinsic roughness, the calipers may measure the most exterior or interior contact points of the composite tube. For a more precise assessment of the cross-sectional dimensions, five specimens were subjected to X-ray computed tomography (XCT)

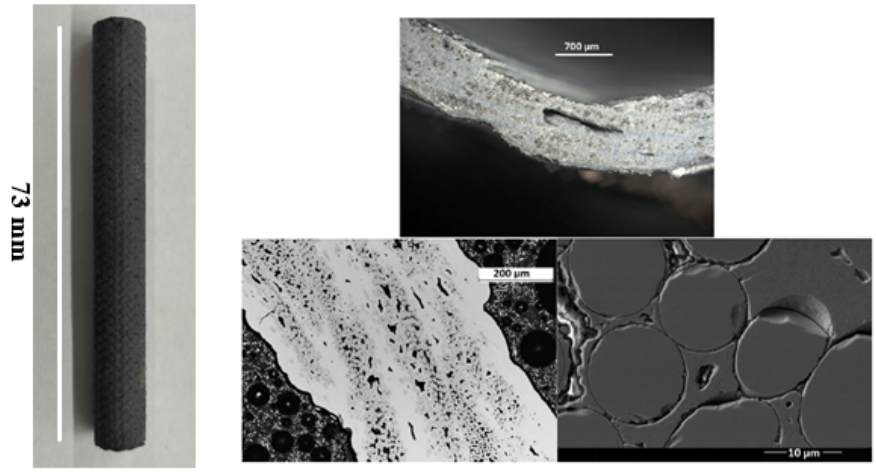

Figure 2.1: Specimen prepared (left) and similar specimen observed by optical microscopy and scanning electron microscopy (right) [3].

analysis. The analysis reported an OD and ID of 9.3 ± 0.2 mm and 8.0 ± 0.2 mm, respectively. This indicates that the caliper-based measurements generally overestimate the cross-sectional area, leading to a relatively conservative value when calculating strength. To rectify this discrepancy, we adjusted the caliper-based cross-sectional measurements of all the specimens by applying the average ratio between the XCT-measured and the caliper-measured cross-sectional areas, based on the five specimens. Fig. 2.1 presents a specimen and the observable architecture, as examined through optical microscopy and scanning electron microscopy [3].

Chapter 3

Multiaxial Experiments for SiC/SiC composites

In this chapter, we introduce our innovative multiaxial testing system crafted specifically for SiC/SiC, designed to facilitate tests across different loading paths. Both strain and Acoustic Emission (AE) outcomes are presented, paired with the criteria utilized for determining PLS. We also show the multiaxial failure surface results and the statistical distribution of PLS. These findings will serve as empirical inputs for the model discussed in subsequent chapters.

3.1 Multiaxial testing system

Following the standards provided by ASTM C1173 [64], various researchers have proposed designs for the uniaxial tension testing of SiC/SiC tubular samples. Due to the brittle nature of the matrix material of SiC/SiC composites, designing end grips that can effectively transmit axial force without inducing significant end

effects is particularly challenging. Some studies used specimens with tapered ends wrapped around conical structures, using split copper collets to ensure specimen grip and alignment [3]. Alternatively, a more straightforward method involves using epoxy at the interface of straight-walled tubes and grip fixtures [11, 10, 8]. For practicality, the present study used the adhesive technique for applying axial loading.

For the hoop tension test, the ASTM C1819 standard [65] recommends the elastomer insert technique. This method involves placing a cylindrical elastomer inside the tubular specimen and subjecting it to axial compression. This compression prompts the elastomer to radially expand, exerting pressure on the internal wall of the specimen. Nevertheless, the elastomer plug could buckle during the loading process. Furthermore, a considerable amount of friction could develop along the interface between the SiC/SiC specimen and the elastomer. Consequently, the elastomer may not be able to exert a uniform hoop stress along the gauge length of the specimen. An alternative approach is to apply internal fluid pressure to the specimen. Since SiC/SiC composites inherently contain pores, effective sealing of the specimen and the interface between the specimen and testing equipment is of paramount importance. Typically, a polymer bladder is inserted into the tube to seal the specimen[11, 8].

In a previous study on multiaxial testing of SiC/SiC tubes [8], the interface between the bladder, specimen, and steel grip relied solely on the use of high-strength epoxy. However, our tension-internal pressure trial experiments showed that, when subjected to intense axial forces, the epoxy is susceptible to leaks,

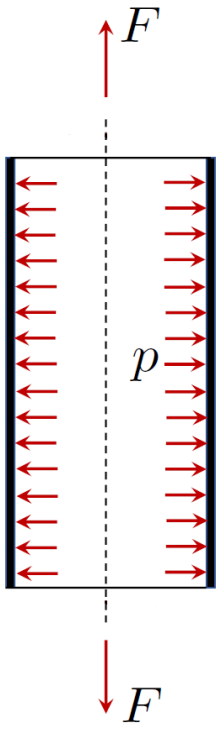

Figure 3.1: Schematic of loading configuration of SiC/SiC cladding.

hindering the specimen from achieving its UTS. Therefore, we designed and fabricated a new multiaxial testing apparatus for a diverse range of load combinations and loading rates. The interest of this study is to investigate the behavior of SiC/SiC specimens under the combination of axial stress and internal pressure, as depicted in Fig. 3.1. The test apparatus can easily be modified to include torsion and external pressure tests.

In the current design, we fabricated Viton membranes with a unique floral shape, which ensures a seal on both the internal surface of the specimen and the interface between the specimen and the testing apparatus. High-strength epoxy (Scotch-Weld Epoxy Adhesive 1838, 3M) was used for transmitting axial loads.

The overall design and components of the apparatus are shown in Fig. 3.2. In the multiaxial experiment, the SiC/SiC specimen was adhered to both the upper and lower steel plates. To prevent any off-center alignment during the epoxy curing process, the specimen and plates were kept in place using an alignment tool, as illustrated in Fig. 3.3. A Viton membrane was inserted through the hole in the lower plate and into the SiC/SiC tube, while its flange was secured by fastening the steel bottom plate to the steel pedestal. Within the steel pedestal, O-rings were installed to obstruct high-pressure liquid from seeping through the interfaces. The specimen and the upper plate were precisely aligned within the steel clamp, and the entire assembly was affixed to the load frame (model 815, MTS Systems). The effective gage length of the specimen was measured to be approximately 40 mm. Based on St. Venant's principle, it can be inferred that the central segment of the specimen is subjected to uniform tensile stress.

3.2 Strain measurement and AE system

In the experiment, 6-mm long strain gages were attached to the outer surface of the specimen in both axial and lateral directions. The strain gages cover several repeating cells of the SiC/SiC composites. The non-flat surface of the woven architecture of SiC/SiC composites makes it difficult to glue strain gages in a single step. The adhesive was first placed on part of the specimen surface and allowed to cure. The hardened epoxy was then lightly sanded and the strain gages were placed on the specimen.

In addition to strain measurements, acoustic emission (AE) was used to monitor damage growth during the loading process. An AE sensor (model Nano-30,

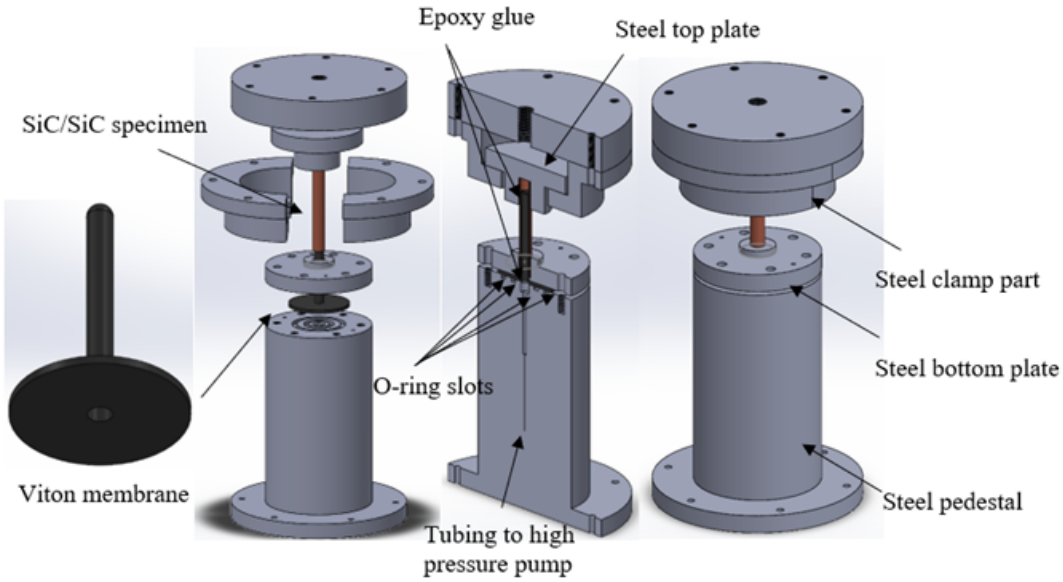

Figure 3.2: Membrane and loading apparatus.

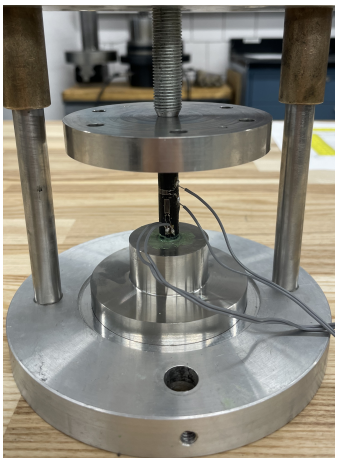

Figure 3.3: Alignment tool.

Physical Acoustics) was attached to the specimen surface using cyanoacrylate adhesive. AE signals were pre-amplified with 40 dB gain and band-pass filtered 0.1-1.2 MHz (model S1220C, Physical Acoustic). One four-channel digitizer (L4534A,

Agilent) with a sampling rate of 20 MS/s, 16 V full-scale range, and 16-bit resolution was used to record the AE signals continuously. A 4000-sample window provides 0.2 milliseconds of recording, with a pre-trigger set at 1500 samples to ensure capturing the first arrival. The digitizers were triggered whenever a selected anchor channel signal reached the amplitude threshold of 25 mV. To avoid one AE event triggering the system twice, a hold-off time of 10 milliseconds between two consecutive events was prescribed. This indicates a maximum AE recording rate of 100 events per second, which is not reached in any of the tests. The time stamps of the trigger were also recorded, which are used for mechanical data analysis. Fig. 3.4 shows the testing and data acquisition system.

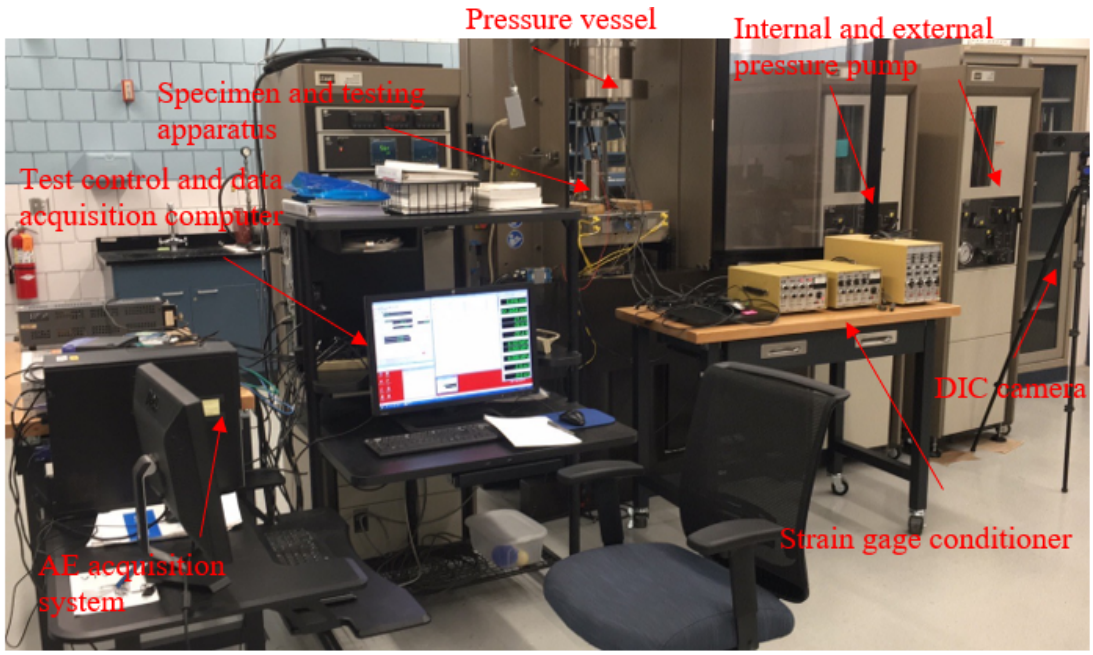

Figure 3.4: Multiaxial testing and data acquisition system.

3.3 Loading protocol

Since the primary interest of the study is to characterize the PLS and UTS, the experiments were performed under load control mode. To investigate the behavior of SiC/SiC specimens under multiaxial stress states, we considered five distinct loading paths: uniaxial tension, hoop tension, equi-biaxial tension, and two other proportional loading paths. To quantify the applied loading, we first define the following nominal stresses:

$$\sigma_{\theta\theta} = \frac{r_i^2(r_m^2 + r_e^2)}{r_m^2(r_e^2 - r_i^2)}p \tag{3.1}$$

$$\sigma_{zz} = \frac{F + p\pi r_i^2}{\pi(r_e^2 - r_i^2)} \tag{3.2}$$

where r_i, r_e are the ID and OD of the specimen, respectively, and $r_m = 0.5(r_i + r_e)$. Note that though these nominal stresses serve as load parameters in the dimension of stress, they physically represent the homogenous elastic stresses of the test specimen. In this study, the loading paths were characterized by the ratio between $\sigma_{\theta\theta}$ and σ_{zz}, i.e. $\sigma_{\theta\theta}/\sigma_{zz} = 0$ for uniaxial tension, $\sigma_{zz}/\sigma_{\theta\theta} = 0$ for hoop tension, $\sigma_{\theta\theta}/\sigma_{zz} = 1$ for equi-biaxial tension, $\sigma_{zz}/\sigma_{\theta\theta} = 2$ and 0.5 for the two unequal loading ratios. For all these loading paths, a constant stress rate of $\dot{\sigma}_{eq} = \sqrt{\dot{\sigma}_{\theta\theta}^2 + \dot{\sigma}_{zz}^2} = 0.1$ MPa/s was prescribed. Based on Eq. 3.1 and 3.2, the rates for axial force $\dot{F}$ and internal pressure $\dot{p}$ were determined for the various loading paths.

3.4 Determination of PLS

Fig. 3.5 presents the stress-strain responses measured for the five loading paths. The Young modulus is taken as the slope of the initial linear region of the stress-strain curve under uniaxial tension. The UTS is determined as the peak stress prior to failure [64, 65]. Following these recommendations, the PLS is determined as the intersection between the stress-strain curve and a straight line with the slope equal to the Young modulus and an offset of 0.01% [4, 11]. However, this method was proposed for uniaxial loading. For multiaxial loading, one would need to consider the nonlinearity of the stress-strain response in both axial and hoop directions.

In this study, we propose the following strain-based criterion in determining PLS for multiaxial stress states:

$$\sqrt{\sum_{i,j}(\epsilon_{ij} - \epsilon_{ij}^{e})^2} = 0.01\% \tag{3.3}$$

where ϵ_{ij} are the measured components of the strain tensor and ϵ_{ij}^{e} are the theoretical elastic strain components calculated as $\epsilon_{ij}^{e} = S_{ijkl}\sigma_{kl}$, where S_{ijkl} = elastic compliance. For the uniaxial tension test, when $\sqrt{\sum_{i,j}(\epsilon_{ij} - \epsilon_{ij}^{e})^2} = 0.01\%$, the lateral strain is very close to that predicted by the elastic solution. Therefore, we have $\sqrt{\sum_{i,j}(\epsilon_{ij} - \epsilon_{ij}^{e})^2} \approx \epsilon_{zz} - \epsilon_{zz}^{e} = 0.01\%$, which is essentially the same as the ASTM recommendation.

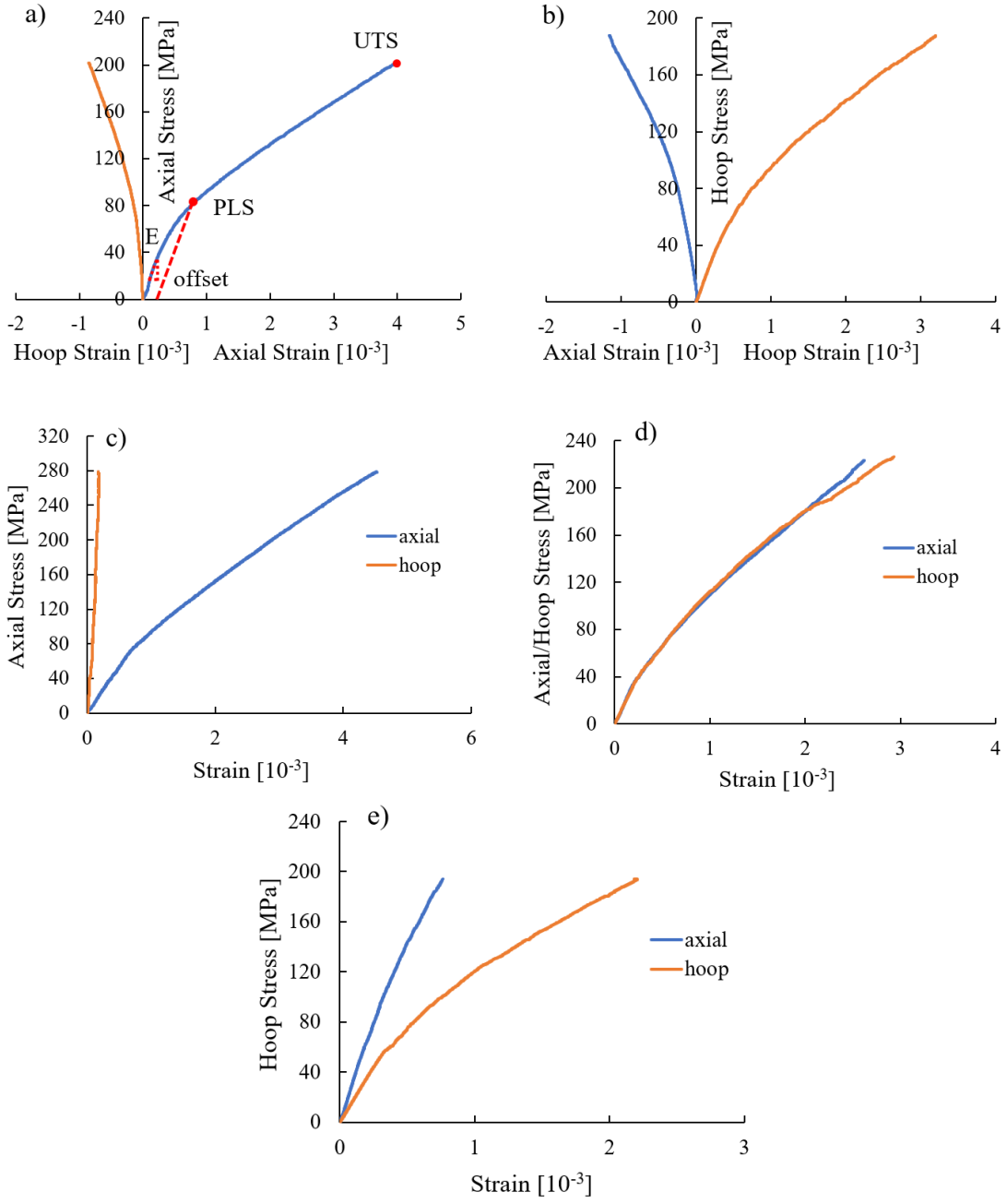

Figure 3.5: Stress-strain responses of five loading paths: (a) uniaxial tension test (with ASTM offset method), (b) hoop tension test, (c) $\sigma_{zz}/\sigma_{\theta\theta} = 2$, (d) biaxial tension test, and (e) $\sigma_{zz}/\sigma_{\theta\theta} = 0.5$.

We further note that Eq. 3.3 is invariant of the coordinate system. To show it, denote the present coordinate system by three orthonormal vectors $\vec{e}_i$ $(i = 1-3)$, and the new coordinate system by vectors $\vec{e'}_i$. The strain tensor in the new coordinate system can be expressed in terms of the present strain tensor

$$\epsilon'_{ij} = a_i^m a_j^n \epsilon_{mn} \tag{3.4}$$

where $a_p^q = \vec{e'}_p \cdot \vec{e}_q$. To express the strain criterion (Eq. 3.3) in the transformed coordinate system, we rewrite Eq. 3.3 by

$$\sqrt{\sum_{i,j} (\epsilon'_{ij} - \epsilon'^e_{ij})^2} = \sqrt{\epsilon'_{ij}\epsilon'_{ij} - 2\epsilon'_{ij}\epsilon'^e_{ij} + \epsilon'^e_{ij}\epsilon'^e_{ij}} \tag{3.5}$$

in which we used the Einstein notation. Following Eq. 3.4, we can write $\epsilon'_{ij}\epsilon'_{ij} = (\vec{e'}_i \cdot \vec{e}_m)(\vec{e'}_j \cdot \vec{e}_n)(\vec{e'}_i \cdot \vec{e}_p)(\vec{e'}_j \cdot \vec{e}_q)\epsilon_{mn}\epsilon_{pq}$. By expressing $\vec{e'}_i = v_k^i \vec{e}_k^i$ and $\vec{e'}_j = v_r^j \vec{e}_r^j$ (no summation on i and j), we have $\epsilon'_{ij}\epsilon'_{ij} = v_k^i v_k^i v_r^j v_r^j \epsilon_{mn}\epsilon_{mn} = \epsilon_{mn}\epsilon_{mn}$. Likewise, we have $\epsilon'_{ij}\epsilon'^e_{ij} = \epsilon_{mn}\epsilon^e_{mn}$ and $\epsilon'^e_{ij}\epsilon'^e_{ij} = \epsilon^e_{mn}\epsilon^e_{mn}$. Therefore, the strain-based criterion (Eq. 3.3) is invariant with the coordinate system.

To further investigate the damage behavior of SiC/SiC specimens at the PLS, we conducted an analysis of the AE measurements collected during the tests. Each test of a SiC/SiC specimen yielded thousands of recorded AE events. Fig. 3.6a presents the AE events per second (commonly referred to as the AE count rate) and the concurrent stress state for a uniaxial tensile test. It was observed that AE events were initiated at the early stages of the loading process, with a notable percentage of the overall AE events occurring prior to the PLS, as determined by Eq. 3.3. In addition, it was discerned that the AE count rate displayed a

gradual escalation, reaching a localized peak in proximity to the strain-defined PLS, followed by a slight reduction marked by pronounced fluctuations. The AE count rate then resumed its upward trajectory as the load approached ultimate failure, culminating in a global peak around the UTS.

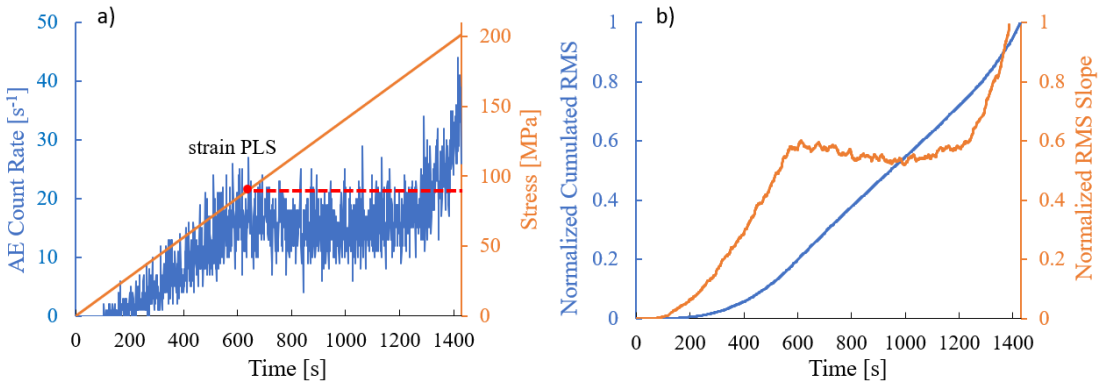

Figure 3.6: (a) Comparison of cumulative RMS and AE count curve, and (b) cumulative AE count curve and its slope from a SiC/SiC multiaxial test.

To highlight the local peak value, we also examine the RMS value in this analysis. The RMS value, defined as the square root of the mean voltage squared under the AE waveform, is calculated for each AE event by

$$RMS = \sqrt{\frac{1}{T}\int_{T_0}^{T_0+T} [V(t)]^2 \mathrm{d}t} \tag{3.6}$$

where $V(t)$ = time history of voltage output, T_0 represents the first arrival time, and the time period T is intended to encompass the P-wave and S-wave while excluding sensor resonance. From the recorded time histories, a time period T of 20 microseconds (equivalent to 400 samples from the first arrival point) is used in Eq. 3.6. For the uniaxial tensile test depicted in Fig. 3.6a, the RMS value

for each AE event is cumulatively added over time, resulting in the formation of the normalized cumulative curve presented in Fig. 3.6b. The slope of this curve is also calculated and plotted. It can be observed that the slope curve exhibits a local peak value during the early loading stage of the test, a phenomenon that aligns with the local peak value of the AE count rate depicted in Fig. 3.6a. Furthermore, other research has also identified a rapid escalation in crack density through DIC analysis in conjunction with AE cumulative hit counts and energy near the PLS [8]. It is speculated that the initial increase in the rate of AE counts signifies the rapid increase in microcracking in the specimen. As a sufficient number of microcracks form, the microcracks start to nucleate into macrocracks, which leads to a pronounced effect on the stiffness of the specimen. Therefore, it is reasonable to use the local peak of the normalized RMS slope to infer the PLS, where we see a clear degradation of the tangential stiffness.

3.5 Mean strength and damage pattern

For each load path, we tested 10 replicates to evaluate the statistics of PLS. For multiaxial loading, the PLS is defined as the value of σ_{zz} or $\sigma_{\theta\theta}$, whichever is larger, when the proposed strain-based criterion (Eq. 3.3) or the AE limit is met. Similarly, the UTS is the peak value of σ_{zz} or $\sigma_{\theta\theta}$, whichever is larger. Table 3.1 presents the mean values and standard deviations (indicated in parentheses) for the AE-based PLS, strain-based PLS, and UTS for all loading paths. Detailed results of the individual tests can be found in the appendix. The measured mean values of the strain-based PLS and UTS for uniaxial tension are close to the reported values (within 10% difference) [4]. The coefficients of variation (COV)

for all the strength measurements in this study ranged from 5.1% to 13.3%.

Loading Paths	**AE PLS [MPa]**	**Strain PLS [MPa]**	**UTS [MPa]**
Uniaxial Tension	90.0 (8.5)	104.3 (8.1)	203.5 (10.5)
Hoop Tension	78.5 (7.0)	102.6 (8.9)	176.9 (15.1)
Biaxial Tension	92.5 (10.2)	113.7 (15.1)	204.3 (10.4)
Multiaxial $\sigma_{zz}/\sigma_{\theta\theta} = 2$	103.2 (10.4)	123.0 (10.3)	265.8 (22.7)
Multiaxial $\sigma_{zz}/\sigma_{\theta\theta} = 0.5$	80.8 (6.9)	131.1 (17.2)	196.8 (22.7)

Table 3.1: Mean and standard deviation (data in parenthesis) of the AE-defined PLS, strain-defined PLS, and UTS for five load paths.

It is seen that, for loading cases, the PLS calculated based on the AE measurement is consistently lower than that calculated from the strain-based criterion. This is because the AE-based PLS is detected earlier in the loading stage compared to the strain-defined PLS. AE-based PLS directly reflects the onset of microcrack formation and nucleation, which serves as the precursor of stiffness degradation, a phenomenon associated with strain-based PLS.

Table 3.1 shows that the mean values of PLS and UTS are highly dependent on the loading path. For instance, the PLS and UTS from the uniaxial tension test are approximately 15% higher than those from the hoop tension test. This indicates the strong anisotropic nature of SiC/SiC composites. The strength in the axial direction is significantly higher than that in the hoop direction due to the higher concentration of fiber tows in the axial direction relative to the hoop direction. It is interesting to note that the difference of the strain-based PLS between axial tension and hoop tension is considerably smaller than that of the AE-based PLS. This can be attributed to the fact that the hoop stress is calculated using the average radius of the tube whereas the strain is measured at the outer surface of the tube. The actual hoop stress at the outer surface would be lower

than that calculated at the average radius.

For the multiaxial loading, the case of $\sigma_{zz}/\sigma_{\theta\theta} = 2$ exhibits the highest values of PLS and UTS. Due to the Poisson effect, the co-existence of loading in both axial and hoop directions alleviates the damage growth in each of these directions. However, we note that the equi-biaxial loading case does not show the maximum PLS and UTS. This indicates that the tow orientation of the test specimen favors the axial loading direction. However, when $\sigma_{\theta\theta}$ diminishes, the loss of the Poisson effect has an adverse effect on the damage resistance in the axial direction, and consequently, the PLS and UTS measured in the axial direction starts to decrease.

Fig. 3.7 illustrates the ultimate failure patterns of the specimens under uniaxial tension, equi-biaxial tension, and hoop tension. When the specimens are subjected to a loading case where $\sigma_{zz} > \sigma_{\theta\theta}$, the resulting failure is characterized by a fracture that is perpendicular to the axial direction, with fibers pulling out from the tow bundles, as illustrated in Fig. 3.7a. In contrast, for specimens loaded with $\sigma_{\theta\theta} > \sigma_{zz}$, a severe fracture occurs from the internal surface and progresses through the entire thickness of the specimen. The internal pressure control mode causes the pressurized fluid to penetrate into the crack, which eventually leads to a loss of structural integrity in the specimen, as illustrated in Fig. 3.7b. In the equal-biaxial tension test, both failure modes are observed, and the final failure pattern is characterized by the formation of both a horizontal failure plane and a hole in the specimens, as illustrated in Fig. 3.7c. The observed variation in failure patterns is the consequence of the differences in the loading directions in relation to the microstructural features of the specimens and affects the strength properties of the specimen.

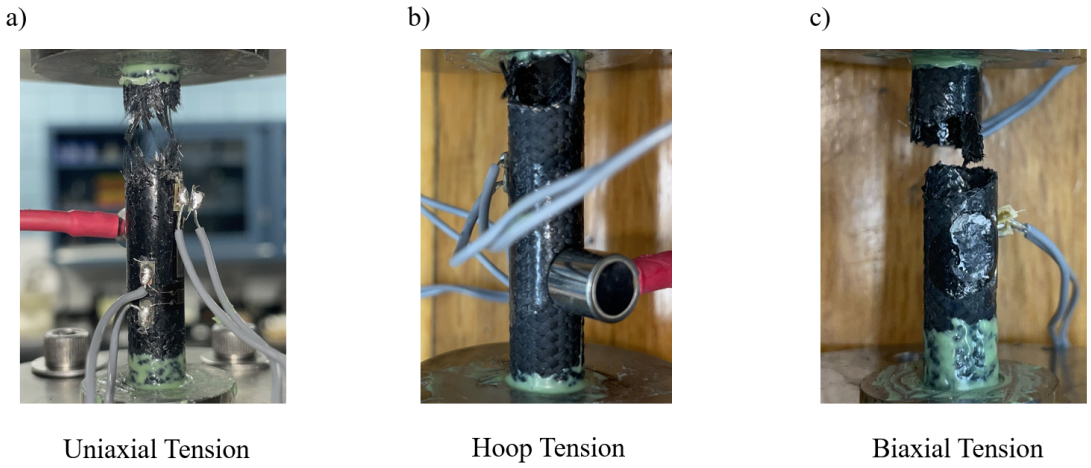

Figure 3.7: Specimen failure patterns for (a) uniaxial tension test (b) biaxial tension test, and (c) hoop tension test.

3.6 Multiaxial failure surface

The results of the multiaxial experiments allow us to plot the failure surface of the SiC/SiC composite specimens. To discuss the failure surface, we first need to define the meaning of failure. For structural design, failure often refers to the attainment of the peak load capacity. At that point, the structure would fail under controlled load. For most structures, as the peak load is reached, the material has already experienced some degree of damage. For fuel claddings, failure can be defined as damage initiation, which could lead to leakage of fission gas. This is not a structural failure but it could cause severe safety consequences of the LWR. In this study, we define material failure as damage initiation, a state corresponding to PLS, which is more stringent than the strength-based failure criterion.

For damage initiation, it suffices to adopt a stress-based failure criterion.

Bernachy-Barbe et al. proposed the following strength-based failure criterion [8]:

$$F(\sigma_i, k_i) = k_1\langle\sigma_1\rangle^2 + k_1\langle\sigma_2\rangle^2 + k_2\langle\sigma_1\rangle\langle\sigma_2\rangle + k_3\sigma_3^2 - 1 \geq 0 \tag{3.7}$$

where σ_1, σ_2 = in-plane principal elastic stresses, $\sigma_3 = \sigma_{\theta\theta} - \sigma_{zz}$, k_i $(i = 1, 2, 3)$ = model constants, and $\langle x\rangle$ = Macaulay bracket= $\max(x, 0)$. It was shown that this failure criterion can well capture the multiaxial failure behavior of SiC/SiC composites with $\pm 45^\circ$ tow orientation [8], which the term $k_3\sigma_3^2$ corresponds to damage of tows oriented at $\pm 45^\circ$. By considering some specific loading scenarios, the constants k_i's can be related to the strengths of the specimen under uniaxial tension, uniaxial compression, and equi-biaxial tension.

For the specimens tested in this study, the tows are oriented at $\pm 55^\circ$, which calls for a more general failure criterion. Here we propose:

$$F(\sigma_i) = \frac{\langle\sigma_{\theta\theta}\rangle^2}{f_{t\theta}^2} + \frac{\langle\sigma_{zz}\rangle^2}{f_{tz}^2} - \frac{\langle\sigma_{\theta\theta}\rangle\langle\sigma_{zz}\rangle}{f_0^2} + \frac{\sigma_{\theta z}^2}{f_\tau^2} - 1 \geq 0 \tag{3.8}$$

where $f_{t\theta}$ = tensile strength in the hoop direction, f_{tz} = tensile strength in the axial direction, f_τ = shear strength, and f_0 can be related to the biaxial strength f_b by considering a biaxial test $\sigma_{\theta\theta} = \sigma_{zz} = f_b$. We have

$$f_0 = (f_{t\theta}^{-2} + f_{tz}^{-2} - f_b^{-2})^{-1/2} \tag{3.9}$$

In the study, we use Eq. 3.8 to describe the failure surface corresponding to PLS. Recent thermo-mechanical elastic analysis of SiC/SiC cladding under a combination of external pressure, internal pressure, temperature, and irradiation-induced swelling showed that the shear stress $\sigma_{\theta z}$ is insignificant as compared to

the axial and hoop stresses [4]. Therefore, we may ignore the shear component in Eq. 3.8, and the failure criterion becomes:

$$F(\sigma_i) = \frac{\langle\sigma_{\theta\theta}\rangle^2}{f_{t\theta}^2} + \frac{\langle\sigma_{zz}\rangle^2}{f_{tz}^2} - \frac{\langle\sigma_{\theta\theta}\rangle\langle\sigma_{zz}\rangle}{f_0^2} - 1 \geq 0 \tag{3.10}$$

From the present experiments, we measured f_{tz}, $f_{t\theta}$, and f_b, and based on Eq. 3.10 we can plot the failure surface. Fig. 3.8 compares the failure surface described by Eq. 3.10 with the measured mean values of both AE-based and strain-based PLS. The good agreement indicates that Eq. 3.10 is sufficient for the PLS failure surface of SiC/SiC composites in biaxial tension (i.e. both $\sigma_{\theta\theta}$, $\sigma_{zz} > 0$).

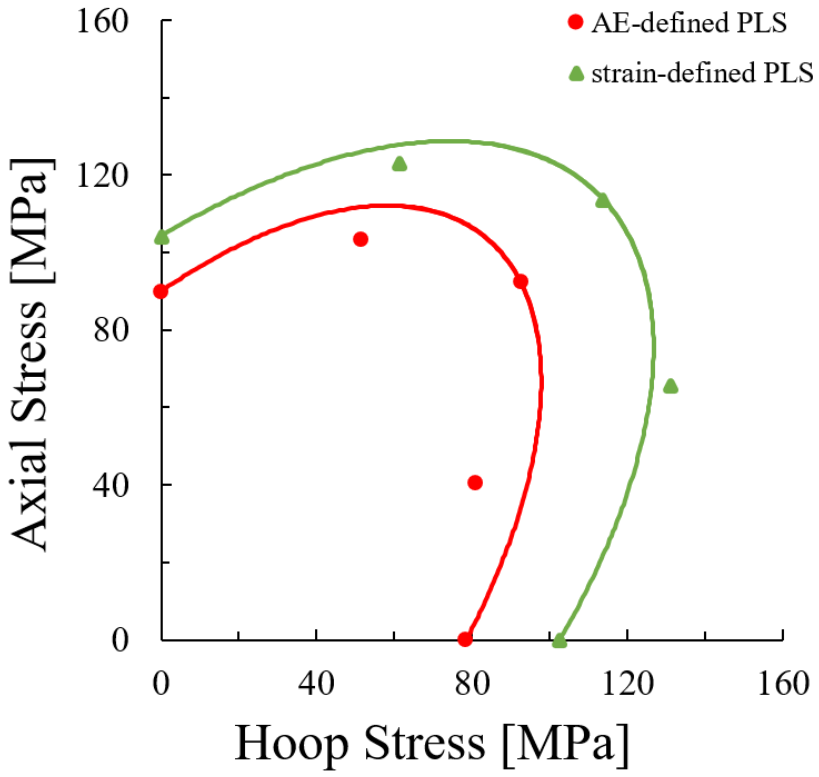

Figure 3.8: PLS failure surface of SiC/SiC composites.

3.7 Probabilistic model of multiaxial PLS

Given that the PLS for SiC/SiC composite cladding corresponds to the damage state at which a gas leak could occur, PLS is generally regarded as an essential design parameter. The previous section discusses the multiaxial failure surface of the mean PLS. Since the present experiments also investigate the variability of PLS, we will now extend Eq. 3.10 to model the statistics of the multiaxial failure surface. Let η denote the PLS for a given loading path. To plot the probability distribution of η, we rank the values of η of test specimens in ascending order, and the corresponding cumulative probability is calculated by

$$p_i(\eta) = (i - 0.5)/n \tag{3.11}$$

where i = rank of strength value η, and n = total number of test specimens. Fig. 3.9 shows the measured probability distributions of η plotted on the Weibull scale, taking strain-defined PLS as an example. Note that, if the data points fall on a straight line, they can be fitted by a two-parameter Weibull distribution. It is seen from Fig. 3.9 that the experimental data cannot be fitted by a straight line. The inapplicability of a Weibull distribution is well expected for quasi-brittle structures since the structure size is not much larger than the zone of damage localization [25, 17].

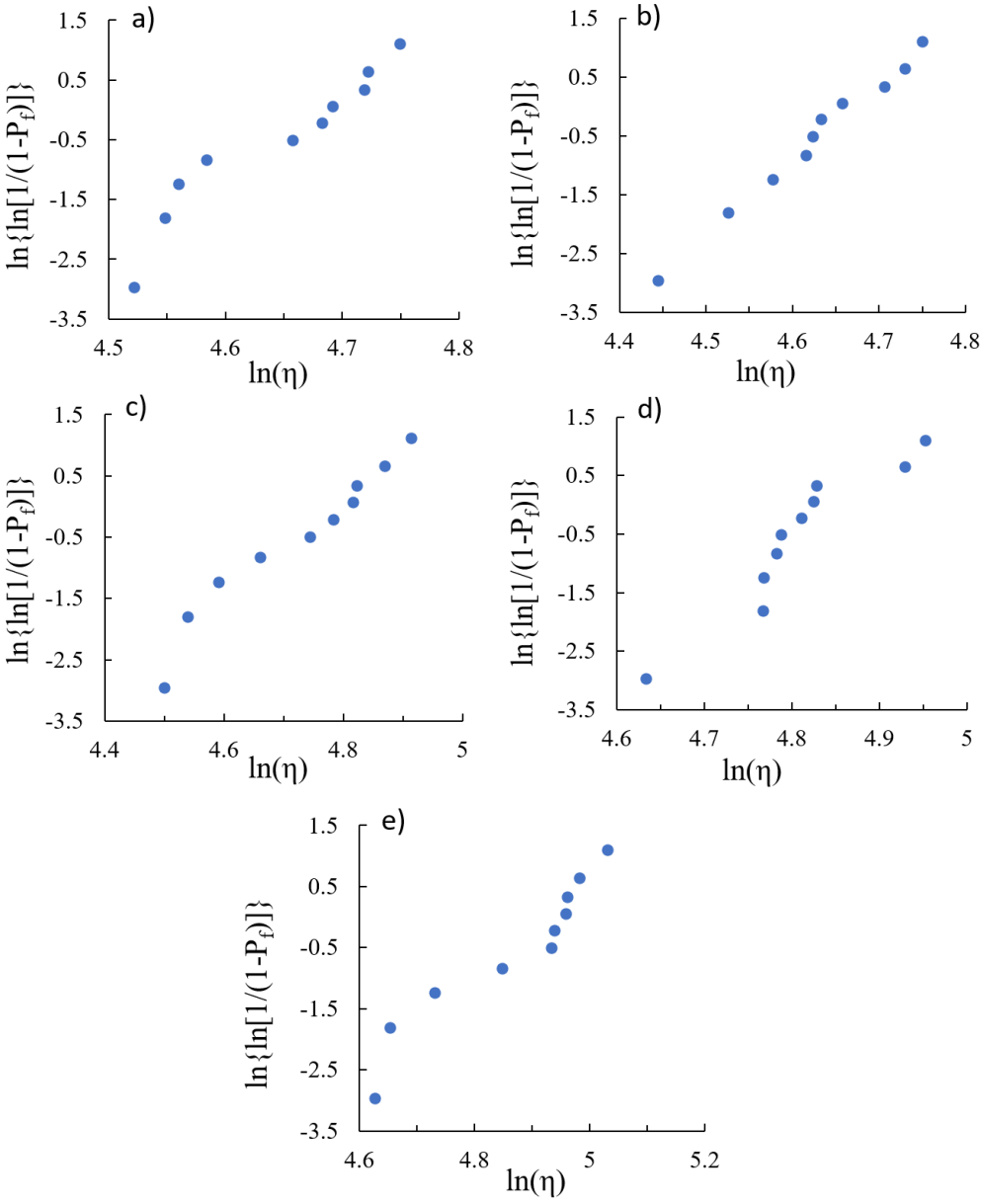

Figure 3.9: Probability distributions of strength in different loading paths: (a) unaxial tension test, (b) hoop tension test, (c) $\sigma_{zz}/\sigma_{\theta\theta} = 2$, (d) biaxial tension test, and (e) $\sigma_{zz}/\sigma_{\theta\theta} = 0.5$.

According to Eq. 3.10, the failure surface can be fully described by three

PLS limits: tensile strength f_{tz} in the axial direction, tensile strength $f_{t\theta}$ in the hoop direction, and biaxial tensile strength f_b. Here we consider these three PLS limits to exhibit certain randomness, and they follow a Gauss-Weibull probability distribution. This distribution function was recently developed for quasi-brittle materials based on atomistic fracture mechanics and a multiscale statistical model [23, 66, 25, 17]. The salient feature of the model is that it captures in the statistical sense both damage localization and load redistribution mechanisms at different scales. The Gauss-Weibull grafted distribution function can be written as

$$F_i(x) = \begin{cases} 1 - e^{(x/s_i)^{m_i}} & (x \leq x_{gi}) \\ P_{gi} + \frac{r_i}{\delta_{Gi}\sqrt{2\pi}} \int_{x_{gi}}^{x} e^{-\frac{(x'-\mu_{Gi})^2}{2\delta_{Gi}^2}} \, \mathrm{d}x' & (x > x_{gi}) \end{cases} \tag{3.12}$$

where subscript $i = tz, t\theta$ and b denote the model parameters for tensile strengths in the axial and hoop directions, and biaxial tensile strength, respectively. m_i and s_i are Weibull modulus and the scale parameter of the Weibull tail; μ_{Gi} and δ_{Gi} are mean and standard deviation of the Gaussian core, if considered extended to $-\infty$; r_i is a scaling parameter required to normalize the grafted cdf such that $F_i(\infty) = 1$; x_{gi} is the grafting point and $P_{gi} = 1 - e^{(x_{gi}/s_i)^{m_i}}$ is the grafting probability, which is typically on the order of 10^{-3} to 10^{-2} [25, 17]. Since the Weibull tail is very short, the mean and standard deviation of the Gaussian core are almost equal to the mean and standard deviation of the corresponding PLS.

In this study, we use Eq. 3.12 to fit the measured histograms of $f_{tz}, f_{t\theta}$ and f_b, as shown in Fig. 3.10. The resulting model parameters are listed in Table

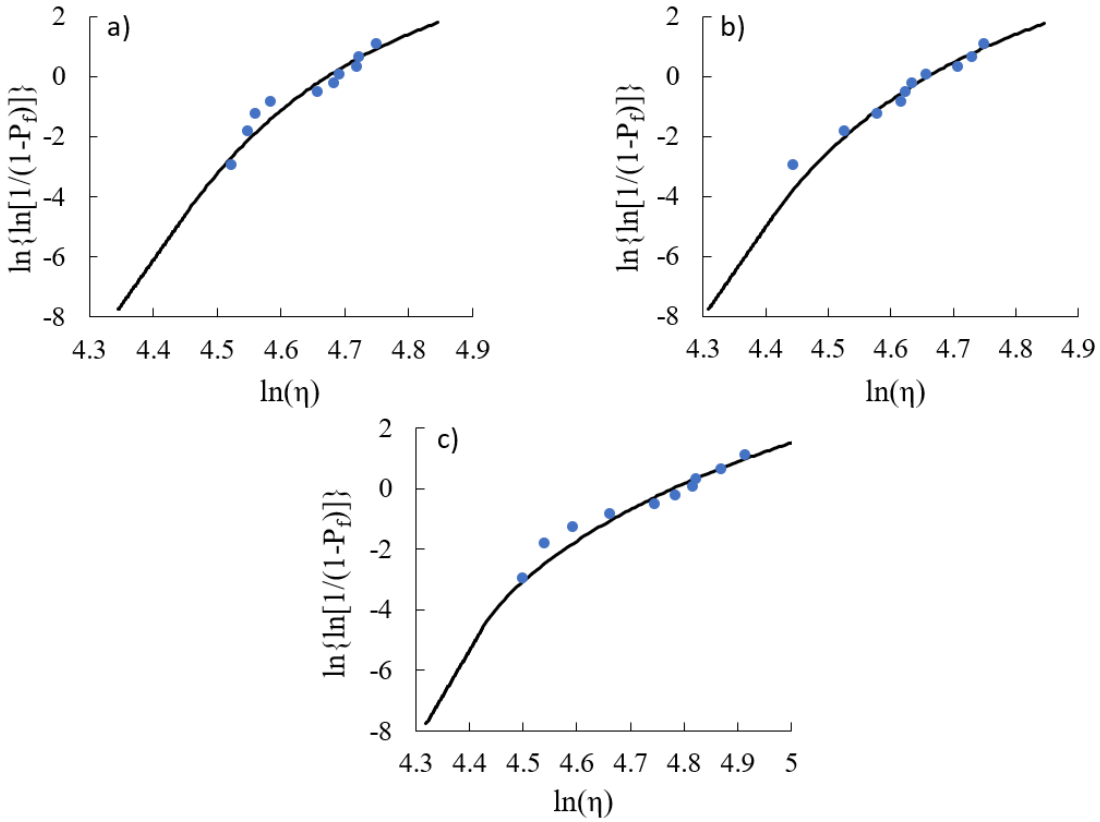

Figure 3.10: Gauss-Weibull fitting of measured histograms of (a)f_{tz}, (b)$f_{t\theta}$, and (c)f_b.

Model Parameters	μ_{Gi}	δ_{Gi}	m_i	s_i	x_{gi}	r_i	P_{gi}
$f_{t\theta}$	104.3	8.1	30	99.9	85.7	1.001	0.01
f_{tz}	102.6	8.9	30	96.3	82.6	1.003	0.01
f_b	113.7	15.1	30	97.3	83.5	1.013	0.01

Table 3.2: Model parameters for fitting histogram of f_{tz}, $f_{t\theta}$, and f_b.

3.2. Once we determine the probability distributions of $f_{tz}, f_{t\theta}$ and f_b, Eq. 3.12 can be used to predict the failure probability for any loading path. Consider a

proportional loading case $\sigma_{\theta\theta} = k\sigma_{zz}$. Based on Eq. 3.10, we have

$$\sigma_{zz} = \left[\frac{k^2}{f_{t\theta}^2} + \frac{1}{f_{tz}^2} - \frac{k}{f_0^2}\right]^{-1/2} \tag{3.13}$$

Based on Eq. 3.9, Eq. 3.13 can be rewritten as

$$\sigma_{zz} = \left[\frac{k^2 - k}{f_{t\theta}^2} + \frac{1-k}{f_{tz}^2} + \frac{k}{f_b^2}\right]^{-1/2} \tag{3.14}$$

With the calibrated probability distributions of f_{tz}, $f_{t\theta}$ and f_b, we can calculate the probability distribution of σ_{zz} through Monte Carlo simulations. Fig. 3.11 shows the comparison between the measured and predicted probability distributions of PLS for loading path $\sigma_{zz}/\sigma_{\theta\theta} = 2$ and $\sigma_{zz}/\sigma_{\theta\theta} = 0.5$. It is seen that they match each other reasonably well. This indicates that Eq. 3.10 is applicable not only to the mean behavior of the failure surface, but also to the statistics of the failure surface. With Eq. 3.10, the statistics of the failure surface can be characterized by the probability distributions of the PLS under uniaxial tension, hoop tension, and equal-biaxial tension.

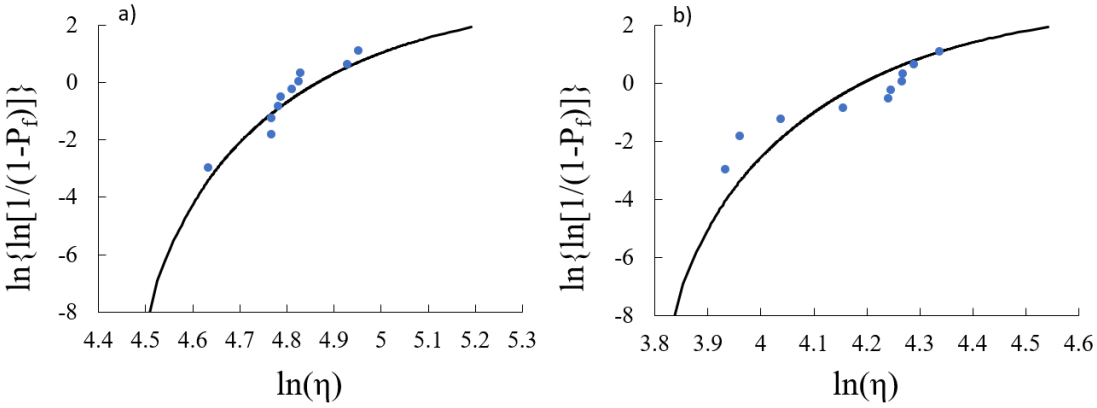

Figure 3.11: Measured and predicted probability distributions of PLS for (a) $\sigma_{zz}/\sigma_{\theta\theta} = 2$, and (b) $\sigma_{zz}/\sigma_{\theta\theta} = 0.5$

Chapter 4

Time-dependent Probabilistic Failure Model

This chapter presents a new stress-based time-dependent multiaxial failure model for the PLS of SiC/SiC materials. The model is further extended to predict the specimen lifetime through a damage kinetics model. By considering the PLS under uniaxial tension in the hoop and axial directions as well as biaxial loading as random variables, the model can be used to calculate the probability distribution of specimen lifetime [67].

4.1 Stress-based failure criterion

From the previous chapter, we have Eq. 3.10 to describe the failure surface corresponding to PLS. Due to the inherent material inhomogeneity, $f_{t\theta}$, f_{tz}, and f_b would exhibit a certain degree of variability. Therefore, they should be considered

as random variables. Consequently, the failure probability of the test specimen under a given loading can be expressed by

$$P_f(\sigma_i) = 1 - \Pr[F(\sigma_i, f_{t\theta}, f_{tz}, f_b) \leq 0] \quad (4.1)$$

$$= 1 - \iiint_{\Omega} f(x_1, x_2, x_3) \mathrm{d}x_1 \mathrm{d}x_2 \mathrm{d}x_3 \quad (4.2)$$

where x_i $(i = 1, 2, 3)$ denote the random values of $f_{t\theta}$, f_{tz} and f_b, respectively, Ω denotes the region of $F(\sigma_i, f_{t\theta}, f_{tz}, f_b) \leq 0$, and $f(x_1, x_2, x_3)$ is the joint probability density function (pdf) of random variables $f_{t\theta}$, f_{tz}, and f_b. In general, the integral in Eq. 4.1 needs to be evaluated numerically.

4.2 Extension to time-dependent failure behavior

The foregoing analysis is anchored by a stress-based failure criterion. In actual applications, the SiC/SiC claddings are subjected to time-dependent loading, which is lower than the load capacity. However, the material could still fail after a substantial period of loading due to subcritical damage growth. In this case, the key design parameter is the structural lifetime or time-to-failure. Therefore, it is necessary to reformulate the failure criterion (Eq. 3.10) for calculating the structural lifetime.

To this end, we consider a damage kinetics model, through which the PLS can be related to the specimen lifetime. Following the framework of continuum

damage mechanics [68, 69, 70], we introduce a damage parameter ω, which ranges from 0 (intact) to 1 (fully damaged). We propose the following kinetics model:

$$\frac{\mathrm{d}\omega}{\mathrm{d}t} = \frac{g^n(\sigma_i)\phi(\omega)}{\langle k - g(\sigma_i)\rangle^n} \tag{4.3}$$

where $g(\sigma) = f_{t\theta}^{-2}\langle\sigma_{\theta\theta}\rangle^2 + f_{tz}^{-2}\langle\sigma_{zz}\rangle^2 - f_0^{-2}\langle\sigma_{\theta\theta}\rangle\langle\sigma_{zz}\rangle$, and k, n are constants. In continuum damage mechanics, a typical choice is $\phi(\omega) = (1-\omega)^{-1}$. Eq. 4.3 is phenomenological in nature, but it reflects the following well-expected behaviors: 1) the damage growth rate is zero in the absence of stress, 2) the damage growth rate increases with the applied stress, and 3) in any case the damage growth rate is non-negative, which signifies the fact that damage growth is irreversible.

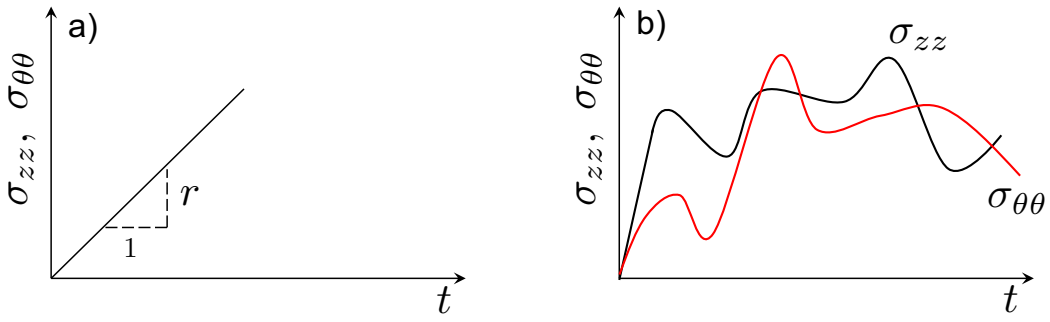

Figure 4.1: Loading protocols: a) reference ramped loading, and b) general loading history.

The damage kinetics model implies that the PLS would depend on the loading rate. Let r denote the loading rates used in the uniaxial tensile experiments in the hoop and axial directions. These experiments directly measure $f_{t\theta}$ and f_{tz}. To

relate the PLS to the specimen lifetime, we now consider two loading protocols: 1) reference linearly ramped loading and 2) general time-dependent loading, as shown in Fig. 4.1. For the reference linearly ramped loading, we consider the case of equal-biaxial loading, i.e. $\sigma_{\theta\theta} = \sigma_{zz} = rt$. By applying the separation of variables to Eq. 4.3, we can express the relation between the damage extent and the by

$$\int_0^{\omega_c} \frac{\mathrm{d}\omega}{\phi(\omega)} = \int_0^{t_c} \frac{\alpha^n t^{2n} \mathrm{d}t}{(k - \alpha t^2)^n} \tag{4.4}$$

where $\alpha = r^2(f_{t\theta}^{-2} + f_{tz}^{-2} - f_0^{-2})$, ω_c = critical damage extent at which the specimen fails under load controlled test, and t_c = time to failure. Meanwhile, the stress-based failure criterion (Eq. 3.10) indicates $\alpha t_c^2 = 1$, or $t_c = \alpha^{-1/2}$. By substituting the expression of t_c into Eq. 4.4, we obtain

$$\int_0^{\omega_c} \frac{\mathrm{d}\omega}{\phi(\omega)} = C/\sqrt{\alpha} \tag{4.5}$$

where $C = \int_0^1 x^{2n}(k - x^2)^{-n}\mathrm{d}x$.

Now consider a general loading history $\sigma_i(t)$ $(i = 1 - 3)$. Applying the same analysis of the kinetics model to this general loading case yields

$$\int_0^{\omega_c} \frac{\mathrm{d}\omega}{\phi(\omega)} = \int_0^{t_f} \frac{\left\{f_{t\theta}^{-2}\langle\sigma_{\theta\theta}(t)\rangle^2 + f_{tz}^{-2}\langle\sigma_{zz}(t)\rangle^2 - f_0^{-2}\langle\sigma_{\theta\theta}(t)\rangle\langle\sigma_{zz}(t)\rangle\right\}^n}{\left\{k - \left[f_{t\theta}^{-2}\langle\sigma_{\theta\theta}(t)\rangle^2 + f_{tz}^{-2}\langle\sigma_{zz}(t)\rangle^2 - f_0^{-2}\langle\sigma_{\theta\theta}(t)\rangle\langle\sigma_{zz}(t)\rangle\right]\right\}^n}\mathrm{d}t \tag{4.6}$$

where t_f = failure time, or the specimen lifetime. We further postulate that, for different loading paths, the specimen would fail at the same critical damage extent. By equating Eqs. 4.4 and 4.6, we obtain

$$\int_0^{t_f} \frac{\left\{f_{t\theta}^{-2}\langle\sigma_{\theta\theta}(t)\rangle^2 + f_{tz}^{-2}\langle\sigma_{zz}(t)\rangle^2 - f_0^{-2}\langle\sigma_{\theta\theta}(t)\rangle\langle\sigma_{zz}(t)\rangle\right\}^n}{\left\{k - \left[f_{t\theta}^{-2}\langle\sigma_{\theta\theta}(t)\rangle^2 + f_{tz}^{-2}\langle\sigma_{zz}(t)\rangle^2 - f_0^{-2}\langle\sigma_{\theta\theta}(t)\rangle\langle\sigma_{zz}(t)\rangle\right]\right\}^n} \mathrm{d}t = C/\sqrt{\alpha} \tag{4.7}$$

From Eq. 4.7, we can solve t_f for any given time-dependent loading. Note that, by using the equivalent damage, the actual form of $\phi(\omega)$ in Eq. 4.3 is not required here. If one wants to quantify the critical damage ω_c at failure, then $\phi(\omega)$ needs to be formulated. By considering $f_{t\theta}$, f_{tz} and f_b as random variables, we perform Monte Carlo simulation to determine the probability distribution of t_f (i.e. lifetime distribution) of the laboratory specimen for a given loading history. The algorithm for calculating this probability distribution is shown below. Note that the probability distribution of t_f exactly equals the failure probability P_{fs} of the specimen at any given time t, i.e. $\Pr(t_f \leq t) = P_{fs}(t)$. What it follows is that the failure probability of the specimen during a particular period of time ($t \in [t_1, t_2]$) can be calculated by $P_{fs} = P_{fs}(t_2) - P_{fs}(t_1)$.

Algorithm 1 Probabilistic Time-Dependent Failure Model Algorithm

```
for Every material element in simulation do
    Find its loading history σ(x, t)
    Array t_f_array = [ ]
    Monte Carlo sampling f_tz, f_tθ, f_b ~ Prob(σ_N)
    for Every sampling of (f_t, f_b, f_c) do
        Calculate its corresponding k_1, k_2, k_3
        Solve t_f based on Eq. 4.7
        Append t_f in t_f_array
    end for
    Sort t_f_array
    Calculate P_fs based on sorted t_f_array
end for
```

Chapter 5

Finite Weakest Link Model for Design Extrapolation

The foregoing chapters focused on the failure of laboratory specimens. The laboratory specimens usually have the same cross-sectional dimension as the fuel cladding, but the specimen length is about two orders of magnitude shorter than the fuel cladding. The essential question is how to predict the failure statistics of the full-size cladding from the laboratory test results. To this end, we need to develop a statistical model that is consistent with the failure mechanism. This chapter will present a finite weakest-link model, which physically represents a damage localization mechanism. The model allows efficient calculations of the lifetime distribution of the actual cladding. One important consequence is that the lifetime distribution of the cladding would exhibit a strong size (length) effect.

5.1 Background on weakest-link model

The simplest statistical theory for structural strength is Weibull's theory. It is based on the infinite weakest-link model, imagined as an infinite chain (Fig. 5.1), in which each link corresponds to one representative volume element (RVE) of the material. The Weibull theory is based on the following two hypotheses:

1. The structure fails if one RVE fails, as implied by the weakest-link model; and

2. the number of RVEs that could trigger the structural failure is extremely large and can be considered as infinite.

The structural geometry for which the former hypothesis is valid is often called the *positive geometry*. The positive geometry is defined as the structural geometry for which the stress intensity factor (or the energy release rate) at constant load increases as the crack grows. For structures under load control, the failure for such geometry occurs right at the beginning of crack propagation. In the opposite case of negative geometry, the structure does not fail when one RVE softens. Rather, the crack extends under an increasing load in a stable manner, as typically seen in reinforced concrete structures and also achieved in some fracture specimens such as a large panel with a small center crack, loaded on the crack, or in a reverse-taper double-cantilever specimen.

Hypothesis 2 means that, in comparison to structure size D, the FPZ is so small that it can be treated as a point. For geometrically similar structures of various sizes, the stress distribution as a function of relative coordinate vector

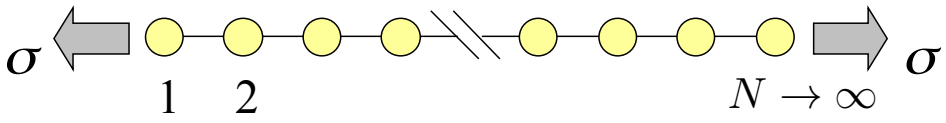

Figure 5.1: Weakest-link model of strength statistics.

$\boldsymbol{\xi} = \boldsymbol{x}/D$ of material points is then independent of D ($\boldsymbol{x}$ = actual coordinate vector).

Hypothesis 2 has often gone unmentioned and has usually been considered automatically applicable. But recently it transpired that, for structures made of concrete, fiber composites, tough ceramics, and other quasi-brittle materials, the number of potentially failing RVEs is often far too small to justify the application of Weibull statistics.

Denote P_k = failure probability of the k^{th} RVE ($k = 1, 2, ...N$) of structure, and P_f = failure probability of the structure as a whole. Since positive geometry is assumed, the structure must fail as soon as one RVE fails. In other words, the structure behaves statistically as a chain, which fails as soon as one link fails (Fig. 5.1). The trick to determine P_f is to switch attention from failure probabilities P_k to survival probabilities, which are $1 - P_k$ for each RVE. Obviously, the structure will survive if all its RVEs survive. So, the probability of survival of the structure is the joint probability of survival of all the RVEs. Thus, if we assume that all P_k are statistically uncorrelated (which is acceptable when the autocorrelation length of the random strength field in the structure is not appreciably larger than the

spacing of the RVEs), we have, according to the joint probability theorem,

$$1 - P_f = (1 - P_1)(1 - P_2) \cdots (1 - P_N) \tag{5.1}$$

$$\text{or} \quad \ln(1 - P_f) = \sum_{k=1}^{N} \ln(1 - P_k) \approx -\sum_{k=1}^{N} P_k \tag{5.2}$$

Here we introduced the small P_k approximation

$$\ln(1 - P_k) \approx -P_k \tag{5.3}$$

because, in a very long chain, $P_k \ll 1$. The reason is that a very long chain is likely to fail at stress that is in the range of very low probability.

5.2 Weibull theory

Based on his experiments of unprecedented scope (not yet surpassed), Weibull [20, 21] realized that to fit his test data, the left (low probability) tail of the cumulative distribution function (CDF) of RVE strength (i.e., failure probability P_k of one RVE) must be a power law[1], i.e.,

$$P_k = [\sigma(\boldsymbol{x}_k)/s_0]^m \qquad \text{for small } \sigma(\boldsymbol{x}_k) \tag{5.4}$$

[1]In 1928, Fisher and Tippet [71], working at Cambridge University, evidently unknown to Weibull, came to the same conclusion by mathematical arguments based on the stability postulate of extreme value statistics (as explained later in this chapter).

Here s_0 (of the dimension of stress) and m (dimensionless) are material constants; s_0 is called the scaling parameter, and m the Weibull modulus (or shape parameter); and $\sigma(\boldsymbol{x}_k)$ is the positive part of the maximum principal stress at a point of coordinate vector $\boldsymbol{x}_k$ (we take the positive part because negative normal stresses do not cause tensile fracture). Substituting Eq. 5.4 into Eq. 5.2 and making the limit transition from a discrete sum to an integral over structure volume V (which is justified if the structure consists of many RVEs each of which is much smaller than D), we get the well-known Weibull probability integral;

$$-\ln(1-P_f) \;=\; \sum_k \left(\frac{\sigma(\boldsymbol{x}_k)}{s_0}\right)^m \;\approx\; \int_V \left(\frac{\sigma(\boldsymbol{x})}{s_0}\right)^m \frac{\mathrm{d}V(\boldsymbol{x})}{{l_0}^{n_d}} \tag{5.5}$$

where n_d = the number of spatial dimensions in which the structure is scaled ($n_d = 1$, 2, or 3). The integrand

$$c_f(\boldsymbol{x}) = \frac{[\sigma(\boldsymbol{x})/s_0]^m}{{l_0}^{n_d}} \tag{5.6}$$

is called the spatial concentration of failure probability and is the continuum equivalent of P_k of one RVE, whose volume is ${l_0}^{n_d}$. Because the structural strength depends on the minimum strength value in the structure, which is always in the low probability range if the structure is large, the validity of Eq. 5.5 for large enough structures is unlimited.

Eq. 5.5 is contingent upon the assumption that the brittle failure of material occurs in tension (rather than shear or a shear-tension combination) and that the random material strength is the same for each spatial direction, i.e., that the strengths in the three principal stress directions are perfectly correlated. Then it

is justified to interpret σ in Eq. 5.5 as the positive part of the maximum principal stress at each continuum point (this stress must be considered as nonlocal when the finite elements are smaller than the RVEs). However, if the random strengths in the principal directions at the same continuum point were statistically independent, then $\sigma^m(x)$ in Eq. 5.5 would have to be replaced by $\sum_{I=1}^{3} \bar{\sigma}_I^m(x)$ where $\bar{\sigma}_I^m(x)$ are the positive parts of the principal nonlocal stresses at that point [72, 73]. Nevertheless, assuming this kind of statistical independence seems unrealistic.

5.3 Scaling of Weibull theory and pure statistical size effect

Consider now geometrically similar structures of different sizes D. In such structures, the dimensionless stress fields $\bar{\sigma}(\boldsymbol{\xi})$ are the same functions of dimensionless coordinate vector $\boldsymbol{\xi} = \boldsymbol{x}/D$, i.e., they depend only on structure geometry but not on structure size D. In Eq. 5.5, we may then substitute

$$\sigma(\boldsymbol{x}) = \sigma_N \bar{\sigma}(\boldsymbol{\xi}) \quad (\boldsymbol{\xi} = \boldsymbol{x}/D) \tag{5.7}$$

where σ_N = nominal stress = P/bD where P is the applied load or a conveniently defined load parameter, and b = structure width (which may but need not be scaled with D). Further, we may set

$$\mathrm{d}V(\boldsymbol{x}) = D^{n_d} \mathrm{d}V(\boldsymbol{\xi}) \tag{5.8}$$

After rearrangements, Eq. 5.5 yields $-\ln(1 - P_f) = (\sigma_N/S_0)^m$ or

$$P_f \;=\; 1-\mathrm{e}^{-(\sigma_N/s_0)^m\Psi(D/l_0)^{n_d}} \;=\; 1 \;-\; \mathrm{e}^{-(\sigma_N/S_0)^m} \tag{5.9}$$

where $$S_0 = s_0(l_0/D)^{n_d/m}\Psi^{-1/m}, \quad \Psi \;=\; \int_V [\bar{\sigma}(\boldsymbol{\xi})]^m \;\mathrm{d}V(\boldsymbol{\xi}) \tag{5.10}$$

According to Eq. 5.9, the tail probability of structural failure is a power law:

$$P_f \;\approx\; (\sigma_N/S_0)^m \qquad (\text{for} \;\; \sigma_N \to 0) \tag{5.11}$$

For $P_f \leq 0.02$ [or 0.2], its deviation from Eq. 5.9 is $< 1\%$ [or < 10 %] of P_f.

The effect of structure geometry is embedded in integral Ψ, which is independent of the structure size. Because exponent m in this integral is typically > 20 (and $0.8^{20} = 0.012$), the regions of structure in which the stress is less than about 80% of material strength have a negligible effect.

Note that P_f depends only on the parameter

$$s_0^* = s_0 {l_0}^{n_d/m} \tag{5.12}$$

and not on s_0 and l_0 separately. So, the material characteristic length l_0 is used here only for convenience, to serve as a chosen unit of measurement. The Weibull statistical theory of strength, per se, has no characteristic length (which is manifested by the fact that the scaling law for the mean strength is a power law [74]).

The last expression in Eq. 5.9 is the Weibull distribution in standard form, with scale parameter S_0. From Eq. 5.10 one finds that

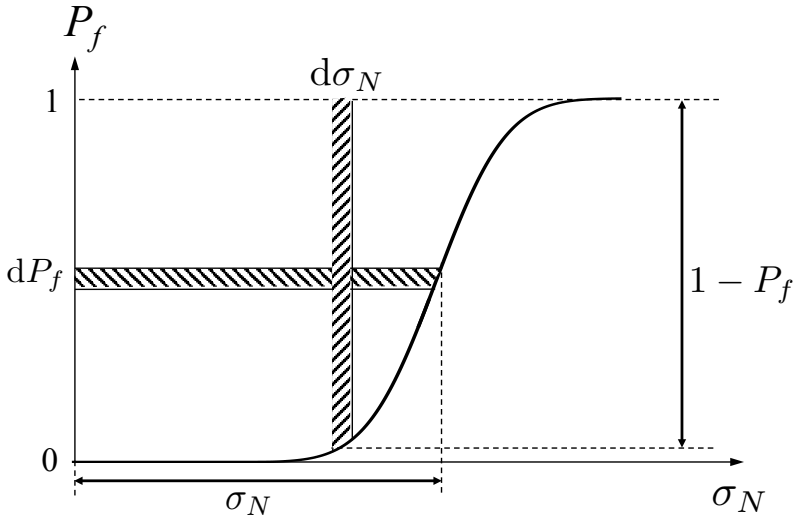

Figure 5.2: Calculation of mean structural strength.

$$\sigma_N \;=\; C_0\ (l_0/D)^{n_d/m} \tag{5.13}$$

where
$$C_0 = C_f \Psi^{-1/m}, \quad C_f = s_0[-\ln(1-P_f)]^{1/m} \tag{5.14}$$

This equation, in which C_0 and S_0 are independent of D, describes the scaling of the nominal strength of the structure when the failure probability P_f is specified.

The mean nominal strength is calculated as (Fig. 5.2):

$$\bar{\sigma}_N = \int_0^\infty \sigma_N p_f(\sigma_N)\mathrm{d}\sigma_N = \int_0^1 \sigma_N \mathrm{d}P_f = \int_0^\infty (1-P_f)\mathrm{d}\sigma_N \tag{5.15}$$

where $p_f(\sigma_N) = \mathrm{d}P_f(\sigma_N)/\mathrm{d}\sigma_N$ = probability density function (PDF) of structural strength, while $P_f(\sigma_N)$ = strength cdf. Substituting Eq. 5.9 and noting that $\int_0^\infty t^{z-1}e^{-t}\mathrm{d}t = \Gamma(z)$ = gamma function, one gets, after rearrangements, the

well-known Weibull scaling law for the mean nominal strength as a function of structure size D and geometry parameter Ψ;

$$\bar{\sigma}_N(D,\Psi) \;=\; s_0\Gamma(1+1/m) \;=\; C_s(\Psi)\; D^{-n_d/m} \tag{5.16}$$

where
$$C_s(\Psi) \;=\; \Gamma(1+1/m)\; {l_0}^{n_d/m} s_0/\Psi^{1/m} \tag{5.17}$$

For the gamma function one may use the approximation $\Gamma(1+1/m) \approx 0.6366^{1/m}$, which is accurate within the range $5 \leq m \leq 50$ (Eq. 12.1.22 in [73]).

The coefficient of variation (CoV) of σ_N is calculated as

$${\omega_N}^2 = {\bar{\sigma}_N}^{-2} \int_0^\infty (\sigma_N - \bar{\sigma}_N)^2 p_f \mathrm{d}\sigma_N = {\bar{\sigma}_N}^{-2} \int_0^\infty {\sigma_N}^2 \; \mathrm{d}P_f(\sigma_N) - 1 \tag{5.18}$$

where $\mathrm{d}P_f(\sigma_N)/\mathrm{d}\sigma_N = p_f(\sigma_N) =$ pdf of σ_N. Substitution of Eq. 5.9 gives, after rearrangements, the following well-known expression for the strength CoV:

$$\omega_N = \sqrt{\frac{\Gamma\left(1+2/m\right)}{\Gamma^2\left(1+1/m\right)} - 1} \tag{5.19}$$

which is independent of structure size as well as geometry. Approximately, $\omega_N \approx (0.462 + 0.783m)^{-1}$ for $5 \leq m \leq 50$ (Eq. 12.1.28 in [73]).

5.4 Finite weakest-link model for SiC/SiC nuclear claddings

The previous sections discussed the infinite weakest-link model for structural strength and the consequent Weibull strength distribution. One important implication of the Weibull strength distribution is the size dependence of strength statistics, often referred to as the Weibull size effect. However, the infinite weakest-link model represents a limiting case, in which the smallest element triggering the failure of the entire structure is far smaller than the overall structure size. This condition is not often met in many practical cases. Therefore, the measured probability distribution of structural strength does not follow the Weibull distribution. In this study, we consider that cladding fails as soon as damage initiates from anywhere. Therefore, the cladding survives if and only if all the material elements survive. Mathematically, the failure statistics of the cladding can be represented by a weakest-link model.

First, consider a laboratory specimen. At failure, the damage would localize into one material element. The size of this material element is related to the width of the fracture process zone. For SiC/SiC composites, the size of the material element which damage localizes is expected to be on the order of the tow width (≈ 1.2 mm). By assuming that the failure statistics of each material element are statistically independent, the failure probability $P_{fs}(t)$ of the specimen subjected to a general loading history can be calculated by

$$P_{fs}(t) = \Pr(t_f \leq t) = 1 - [1 - P_1(t)]^{n_s} \tag{5.20}$$

where $P_1(t)$ = failure probability of one material element, and n_s = number of material elements in the specimen. Eq. 5.20 is written by assuming that all the material elements experience the same stress history up to failure. It is noted that in laboratory testing we normally cannot directly obtain the strength distribution P_1 of one material element. Instead, we can measure the failure probability of a specimen, from which we infer $P_1(t)$ as

$$P_1(t) = 1 - [1 - P_{fs}(t)]^{1/n_s} \tag{5.21}$$

Now consider an actual SiC/SiC cladding. Recent studies have shown that during its service lifetime the cladding experiences a non-uniform stress distribution [4]. To account for the non-uniformity of the stress field, we can write the finite weakest-link model as

$$P_f(t) = 1 - \prod_{j=1}^{n} [1 - P_1(\boldsymbol{\sigma}_j, t)] \tag{5.22}$$

where n = number of material elements in the cladding, and $\boldsymbol{\sigma}_j$ = a vector containing the stress components σ_i for jth material element. Eq. 5.22 can be conveniently rewritten by taking the logarithmic, which will allow us to replace the product by a summation, i.e.

$$\ln [1 - P_f(t)] = \sum_{j=1}^{n} \ln [1 - P_1(\boldsymbol{\sigma}_j, t)] \tag{5.23}$$

Since there are many elements in the cladding, we can replace the summation by integration. Eq. 5.23 can be rewritten as

$$P_f(t) = 1 - \exp\left\{\frac{1}{V_0}\int_V \ln\left\{1 - P_1[\boldsymbol{\sigma}(x,t),t]\right\} \mathrm{d}V\right\} \tag{5.24}$$

where V_0 = volume of one material element. By substituting Eq. 5.21 into Eq. 5.24, we have

$$P_f(t) = 1 - \exp\left\{\frac{1}{V_s}\int_V \ln\left\{1 - P_{fs}[\boldsymbol{\sigma}(x,t),t]\right\} \mathrm{d}V\right\} \tag{5.25}$$

where V_s = volume of laboratory test specimen. $P_{fs}[\boldsymbol{\sigma}(x,t),t]$ represents the failure probability of the test specimen at time t when subjected to stress history $\boldsymbol{\sigma}(t)$ that is experienced by a material point located at x of the actual cladding. As mentioned in Chapter 2, $P_{fs}[\boldsymbol{\sigma}(x,t),t]$ can be calculated through Monte Carlo simulations based on the known cdf's of f_{tz}, $f_{t\theta}$ and f_b through Eq. 4.7.

Eq. 5.25 provides a closed-form relationship between the failure statistics of the test specimen and the full-size cladding. The model has two important features:

- The model captures the effect of cladding length on the failure probability of the cladding. It is well expected that similar to the infinite weakest-link model, Eq. 5.25 would predict a strong length effect on the failure probability of the cladding. Understanding this size effect is essential for design extrapolation across claddings of different lengths.

- The model takes into account the effect of the time-varying load history. It is noted that the use of $P_{fs}[\boldsymbol{\sigma}(x,t),t]$ indicates that the failure probability at any given time depends on not only the current stress state but also the previous load history. This dependence arises from the damage kinetics model, which naturally captures the effect of the load path on the damage

accumulation.

Chapter 6

Reliability Analysis of SiC/SiC Claddings

The present model is applied to evaluate the reliability of SiC/SiC claddings. The purposes of this analysis are 1) to demonstrate the application of the model for reliability analysis of full-length claddings, 2) to investigate the effect of cladding length on the failure probability, and 3) to understand the effect of subcritical damage growth on the failure probability.

6.1 Description of analysis

The stress history used in the analysis was extracted from a recent thermo-mechanical analysis of SiC/SiC cladding [4]. The analysis is concerned with a 4m long SiC/SiC composite cladding under a service lifetime of 2 years. The cladding is subjected to a combination of external pressure, internal pressure,

temperature, and irradiation-induced swelling. The external pressure is kept at 15 MPa over the entire period of time whereas the internal pressure increases linearly from 1 MPa to 20 MPa. The thermal loading is applied to both the internal and external surfaces. The linear heating rate varies along the cladding height. The details of the thermal loading and boundary conditions can be found in [4]. The irradiation dose increases linearly from 0 to 6 dpa over the 2-year period. In the analysis, the constitutive behavior of the SiC/SiC material is described by an anisotropic constitutive model, in which the elastic stiffnesses degrade with the irradiation-induced swelling. In addition, the constitutive model also takes into account the temperature-dependent thermal expansion and conduction.

The numerical analysis showed that the cladding experiences compressive stresses in both axial and hoop directions at the beginning due to external pressure. During this early loading stage, the compressive axial and hoop stresses at the inner region of the cladding are higher than those at the outer region since the inner surface is subjected to a higher temperature than the outer surface. As the loading proceeds, the cladding experiences irradiation-induced swelling. The amount of swelling is strongly dependent on the temperature. The non-uniform spatial distribution of temperature leads to a spatial variation of swelling in the cladding, which drives the evolution of the internal stress distribution. The simulation showed that, over the service lifetime, the hoop stress at the inner surface changes from 152 MPa in compression to 73 MPa in tension and the axial stress rises from 88 MPa in compression to 51 MPa in tension. The change of stresses at the outer surface is less significant. Fig. 6.1 shows the time evolution of the axial and hoop stresses at the inner layer of the cladding at its mid-height. It

is seen that the hoop stress increases at a rate much larger than the axial stress does, as predicted by the elastic solution of the hoop and axial stresses of thin-wall structures.

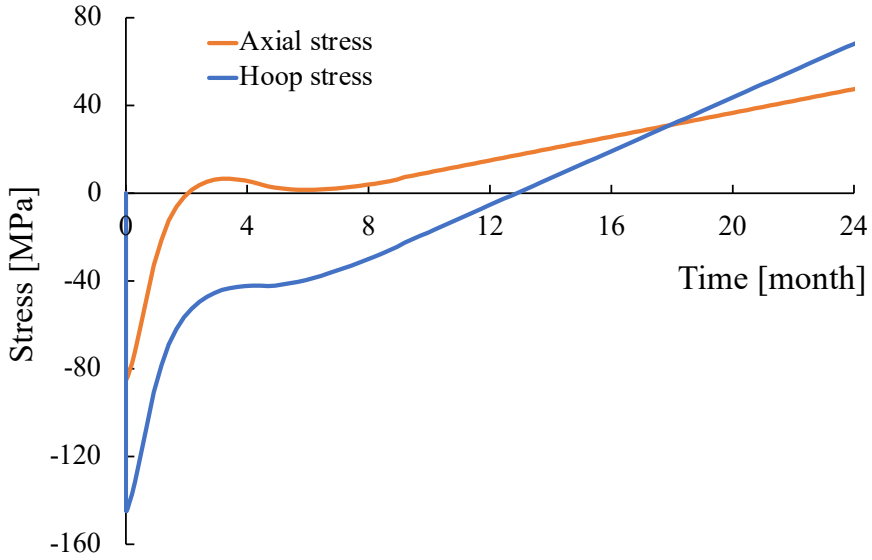

Figure 6.1: Time histories of axial and hoop stresses of the inner layer of the cladding at its mid-height [4].

Over the majority of the loading duration, the inner region of the cladding experiences axial tension, and the hoop stress also turns to be tensile after 12 months. By contrast, the outer region is primarily under mild compressive stresses as compared to the material compressive strength. Fig. 6.2 shows the variation of axial and hoop stresses at the inner surface along the height of the cladding at the end of loading. It is seen that the cladding experiences uniform stress along its

height except towards the two ends. The drastic change of axial stress at the two ends is attributed to the lower temperature, which affects the irradiation-induced swelling.

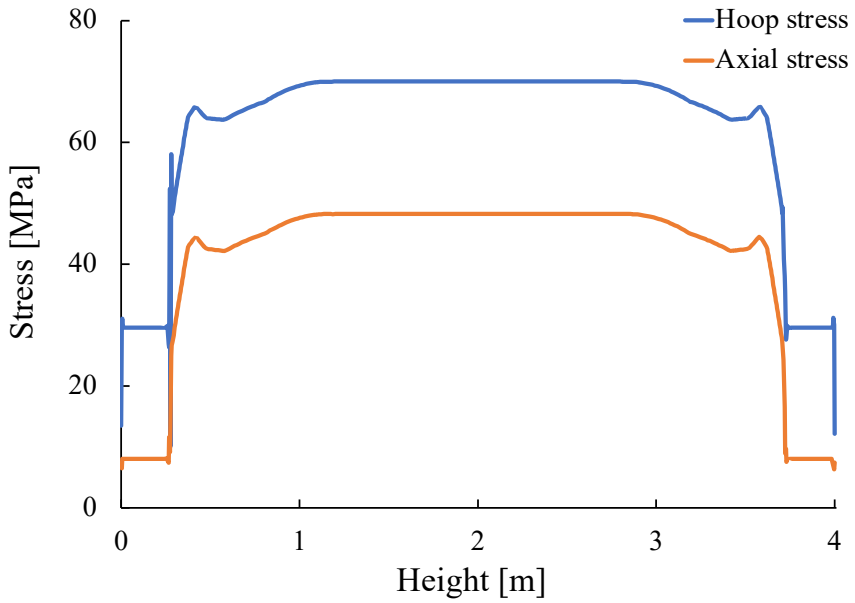

Figure 6.2: Spatial distribution of axial and hoop stresses at 2 years of service along the height of the cladding [4].

Based on the stress history of the cladding simulated in this recent study [4], we calculate the in-plane principal stresses, which are input to the present probabilistic model. As discussed in Sec. 3.5, the probability distributions of PLS limits f_{tz}, $f_{t\theta}$, and f_b are considered to follow a Gaussian-Weibull grafted distribution, and the statistical parameters are determined by the multiaxial tests. By knowing these distribution functions, we can calculate the failure probability of the cladding at any given time during the loading process. Since the stress

histories are calculated by a finite element analysis [8], it is natural to rewrite Eq. 5.25 by

$$P_f(t) = 1 - \exp\left\{\frac{1}{V_s}\sum_j \ln\left\{1 - P_{fs}[\boldsymbol{\sigma}_j(x,t),t]\right\}\Delta V_j\right\} \tag{6.1}$$

where $\boldsymbol{\sigma}_j$ = stress tenor of finite element j and ΔV_j = volume of finite element j. Based on Eq. 4.7, it is not possible to obtain a closed-form solution for $P_{fs}[\boldsymbol{\sigma}_j(x,t),t]$. Therefore, we rely on Monte Carlo simulations to evaluate the failure probability P_{fs} of each finite element. For any given finite element, we first sample the uniaxial tensile and compressive strengths and biaxial tensile strength by

$$f_i = F_i^{-1}(u_i) \quad (i = tz, t\theta, b) \tag{6.2}$$

where u_i = sampled value of a random variable u that is uniformly distributed over the range of 0 to 1. For a given set of $f_{tz}, f_{t\theta}, f_b$ and the stress history, the time-to-failure t_f of each element can be determined from Eq. 4.7. By repeating this calculation for a large number of realizations of $f_{tz}, f_{t\theta}, f_b$, we can calculate the failure probability P_{fs}. The simulated failure probabilities of finite elements are then input to Eq. 6.1 for determining the failure probability of the entire cladding.

6.2 Time evolution of failure probability

In the recent FE analysis, the cross-section of the cladding is discretized into 6 layers in the radial direction. The thermomechanical loading and irradiation

cause a strong non-uniform stress distribution across these layers. In this section, we first analyze the time evolution of the failure probability of the inner layer of the cladding. The simulation results showed that a large part of the inner layer experiences a uniform stress distribution except for the end regions [4]. Here we consider a uniform stress distribution for the inner layer along the cladding height. For the later analysis of the failure risk of the cladding, the actual stress profile will be used.

Fig. 6.3 shows the calculated failure probability of the inner layer. It is seen that the failure probability increases monotonically over time. As mentioned earlier, the failure probability $P_f(t)$ is defined by $P_f(t) = \Pr(t_f \leq t)$. Physically it represents the failure probability of the structure taking into account the entire loading history up to time t. For a given loading history, $P_f(t)$ is a monotonic non-decreasing function. In the present study, the accumulative effect of the past loading history on the failure probability is captured by the damage accumulation model. The failure probability of the structure during a time period $\delta t = t_2 - t_1$ can then be calculated by $P_f(\delta t) = P_f(t_2) - P_f(t_1)$.

Fig. 6.4 presents the time evolution of the contribution of the applied stress on the damage growth by using the mean values of f_t and f_c. As indicated by Fig. 6.1, during the first 8 months, the material experiences compressive stresses in both axial and hoop directions. However, the absolute difference in the in-plane principal stresses is very small as compared to the compressive strength. Therefore, the risk of compression-induced shear failure is negligibly small and the damage growth rate is very low. After 13 months, both axial and hoop stresses become tensile leading to the acceleration of the damage growth. However, the

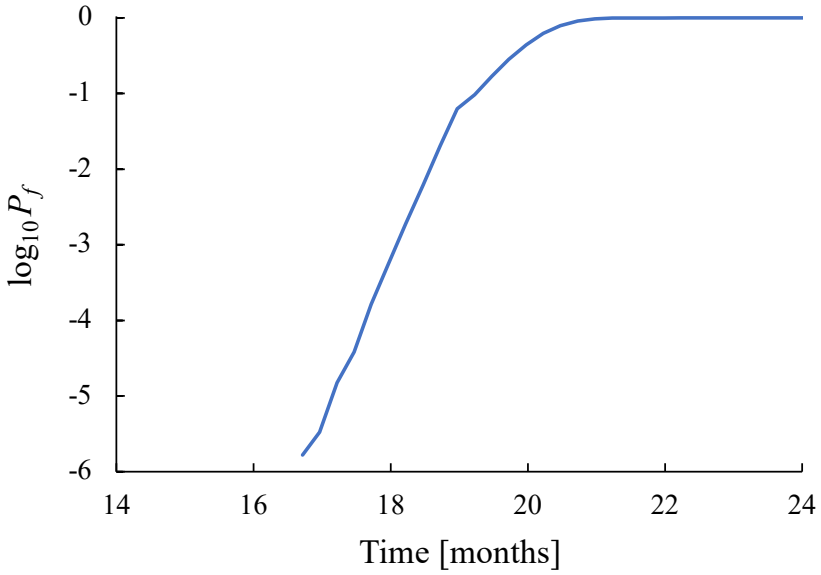

Figure 6.3: Failure probability of the inner layer of the cladding calculated using the stresses at its mid-height.

difference between the hoop and axial stresses decreases, which leads to a decrease in the failure risk. After 18 months, the tensile axial and hoop stresses continue to grow, and meanwhile, the difference between these stress components starts to increase. This causes a considerable increase in the damage growth rate.

The foregoing analysis of the time history of damage growth is directly reflected by the time evolution of failure probability. It is seen that failure probability is relatively small ($< 10^{-5}$) for the first 17 months. Over the last 6 months, the failure probability increases quickly to 1. This is due to the fact that during that period both the axial and hoop stresses increase to a considerable level as compared to the tensile strength of the material.

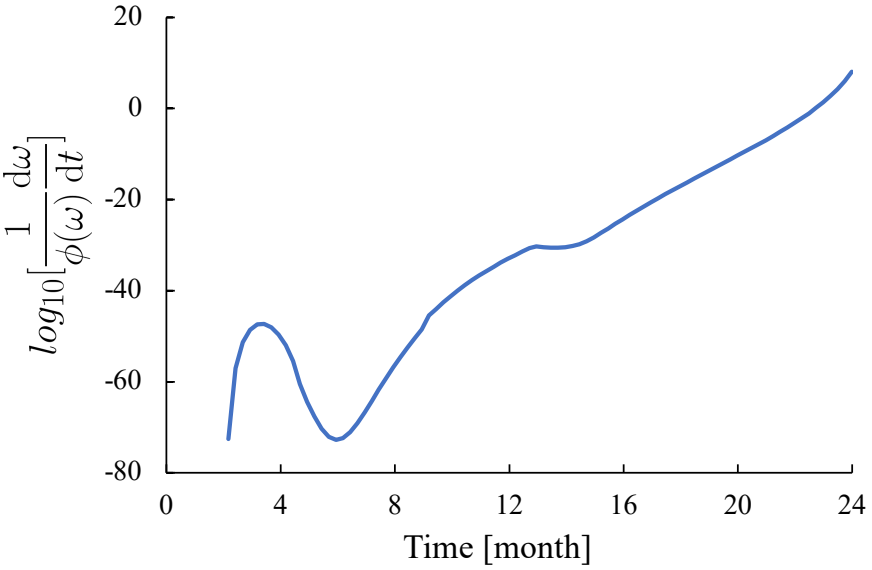

Figure 6.4: Time evolution of contribution of applied stress on the damage growth at the mid-height of the inner layer.

6.3 Spatial distribution of failure probability

It is also of practical interest to investigate the spatial distribution of failure probability. This information not only reveals the most vulnerable part of the structure, but also has profound implications for the scale effect on the failure probability. Based on the stress histories calculated from the finite element analysis [4], we determine the spatial distribution of failure probability P_f of one column of finite elements of the inner layer at the 24th month of service, as shown in Fig. 6.5.

It is seen that the failure probability of material elements is nearly constant over the entire cladding except for the two end regions. This is consistent with the spatial distribution of the stress profile as shown in Fig. 6.2. This indicates that

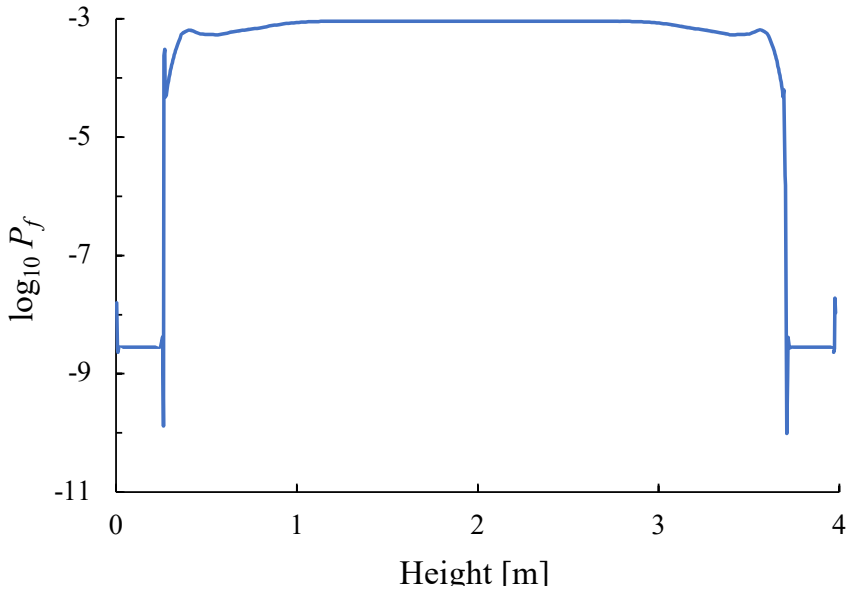

Figure 6.5: Spatial distribution of failure probability of one column of inner-layer elements over a period of 24 months.

the damage has an equal likelihood to occur at any location over the 3m length of the cladding. The uncertainty of the potential damage location indicates a strong weakest link effect on the overall failure statistics. The direct consequence is that the failure probability of the layer would increase with the length of the cladding. Moreover, the type of failure probability function could vary with the cladding length [17]. This size effect must be taken into account in the reliability-based design of the cladding. By contrast, if the layer experiences a strongly non-uniform stress distribution, then the failure location could be deterministic. In this case, the failure probability of the layer is determined solely by the particular material element at the failure location, and therefore the failure statistics are independent of the cladding length.

6.4 Failure probability of entire cladding and the effect of damage growth rate

Fig. 6.6 presents the evolution of the failure probability of the entire cladding over its service period calculated based on the stress histories reported in [4]. It is seen that the failure probability of the cladding grows monotonically over time up to 5.2%. The FE stress analysis showed that the outer layer of the cladding primarily experiences compressive stresses in both hoop and axial directions over the entire loading period, whereas the hoop and axial stresses of the inner layer change from compression to tension as loading proceeds [4].

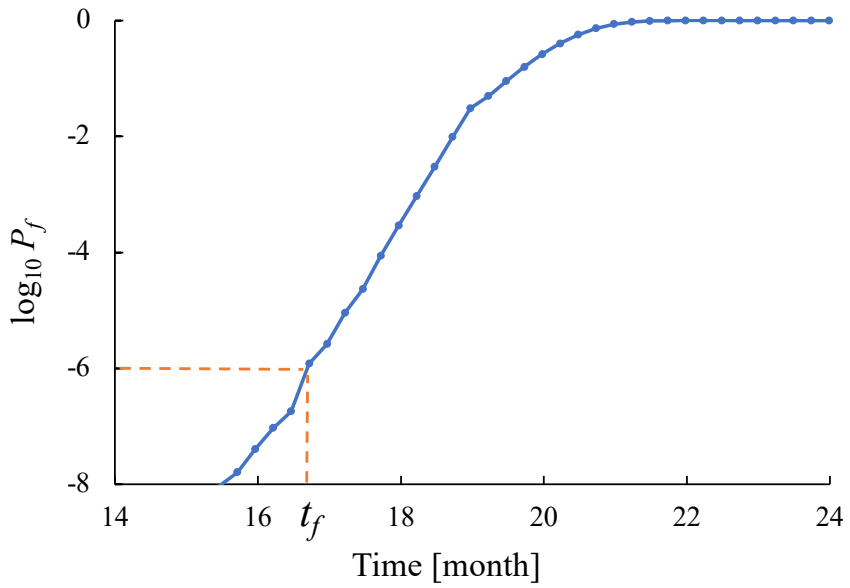

Figure 6.6: Lifetime distribution of the entire cladding; for a tolerable failure risk of 10^{-6}, the cladding should be inspected after $t_f = 16.6$ months of service.

During the first 18 months of service, the entire cladding experiences compressive stresses. Based on the failure criterion, this could lead to compression-induced shear. In this case, the entire cross-section of the cladding contributes to the failure probability. This explains why the failure probability of the cladding is higher than that of the inner layer for the first 18 months. Nevertheless, it should be pointed out that the inner layer experiences higher compressive stresses as compared to the outer layer, and therefore the inner layer is more vulnerable than the outer layer during the early stage of the loading process. After 18 months, the inner layer of the cladding starts to experience tension. Since the compressive strength is considerably higher than the tensile strength, the tensile stresses experienced by the inner layer give rise to a significant level of failure probability. By contrast, the risk of failure due to the compression-induced shear is very low. Consequently, the overall failure probability of the cladding at the end of its service is primarily governed by the inner layer.

Fig. 6.6 provides critical information on when inspection and maintenance are needed to guard against a given tolerable failure risk. Based on Fig. 6.6, for a tolerable failure risk of 10^{-6}, the cladding should be inspected after 16.6 months of service. The present model also shows that the inner surface is the most vulnerable part of the cladding. Therefore, the inspection should focus on the inner surface of the cladding along its entire height.

It is evident that one important component of the present model is the kinetics of damage growth (Eq. 4.3). In this kinetics model, the dependence of the damage growth rate on the applied loading is governed by the exponent n in Eq. 4.3. Fig. 6.7a shows a parametric study on how the value of n influences the time evolution

of the failure probability. It is seen that with an increasing value of n the failure probability of the entire structure decreases. This is because, as n increases, the damage growth rate decreases and so does the failure probability. Fig. 6.7a also includes the failure probability calculated from the time-independent model. In this model, the overall failure statistics of the cladding are still represented by the weakest-link model (Eq. 6.1), but the failure probability function P_{fs} is calculated solely based on the current stress state using Eq. 4.1. As compared to the present time-dependent model, the key difference is that the time-independent model ignores the damaged state of the material and treats the material as in the virgin state for the current loading state. This is an oversimplification, which can cause a gross underestimation of the failure risk. The present model keeps track of the damage state through the damage accumulation model and therefore would predict a higher failure risk than the time-independent model.

Fig. 6.7b shows the lifetime of the cladding for the failure risk of 10^{-6}. It is seen as n-value varies from 50 to 5, and the service lifetime of the cladding decreases from 17 months to 12 months. This indicates the significant influence of the n value on the prediction of the lifetime distribution of the cladding. Therefore, it is crucial to experimentally determine the parameter n. One method is to perform the strength test using a linear ramped loading and the lifetime test using static fatigue on the same batch of specimens. Based on the measured strength and lifetime, Eq. 4.7 can be used to determine the value of n.

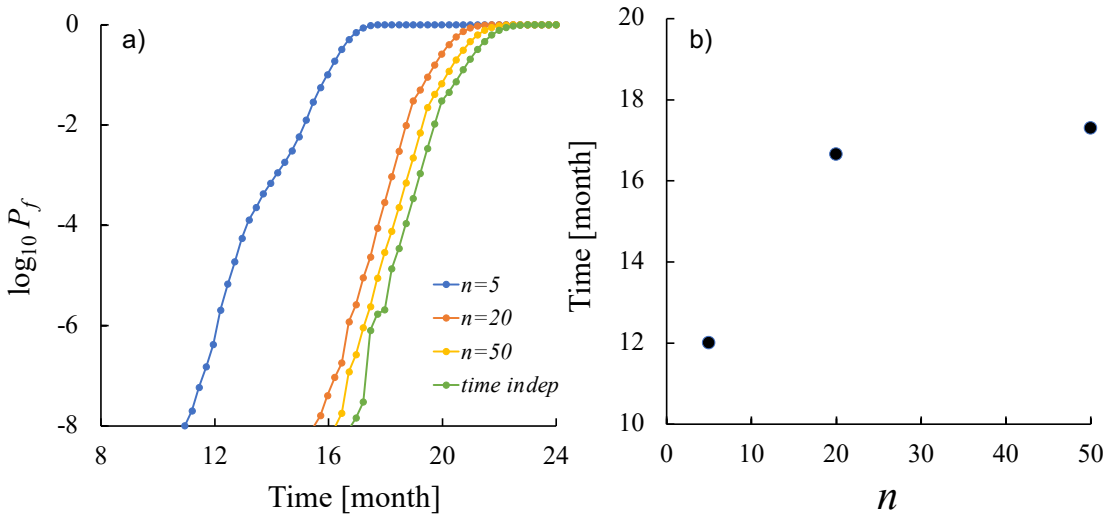

Figure 6.7: (a) Lifetime distributions of cladding calculated by using different n values and a time-independent model, and (b) the corresponding service lifetimes corresponding to $P_f = 10^{-6}$.

6.5 Effect of the cladding length to failure probability

The actual cladding in LWR is around 4m long, which makes it difficult to perform direct mechanical tests. Therefore, it is customary to test specimens of shorter lengths. The essential question for design is how to extrapolate the laboratory test results to a full-length design. To facilitate this design extrapolation, we investigate the effect of the cladding length on the failure probability. Since the failure probability is calculated based on the elastic stress analysis, the stress distribution is independent of the cladding length.

Fig. 6.8 presents the calculated failure probability of claddings of different

lengths. The failure probability of the cladding increases with the increasing length. At a given time, the failure probability of a cladding of 4 m long could be twice the failure probability of a 1m cladding. This difference would be much more pronounced if we compare claddings with a larger length ratio. This behavior is due to the fact that the failure of the cladding is governed by the weakest element. Since most of the cladding experiences a uniform stress distribution, a longer cladding would have a large likelihood of containing weaker elements and consequently a higher failure risk. This is a classical feature of the weakest link statistical model.

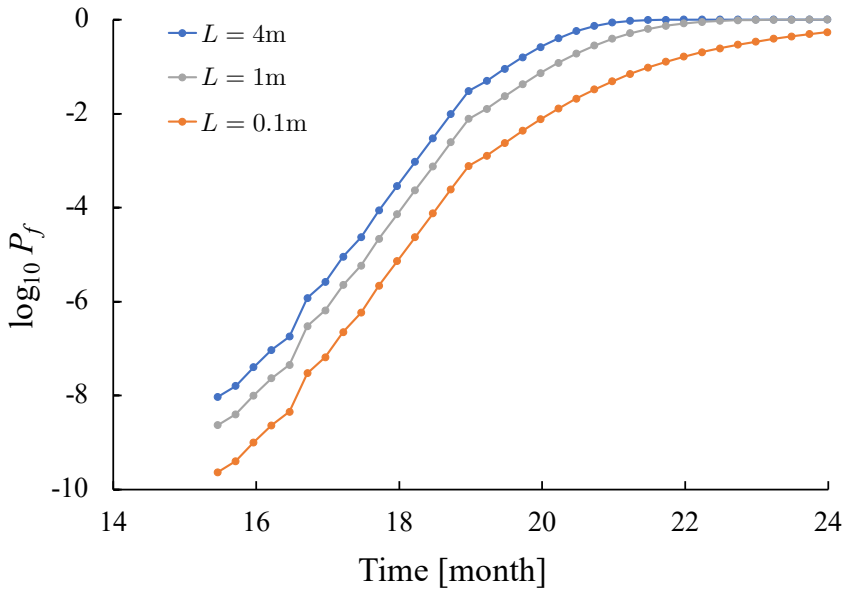

Figure 6.8: Length effect on the failure probability of the cladding.

Fig. 6.9 shows the relationship between the service lifetime corresponding to a failure probability of 10^{-6} and the cladding length. The lifetime of a 4m cladding is 16.7 months while that of a 1m cladding is 17.6 months. This is a strong size effect

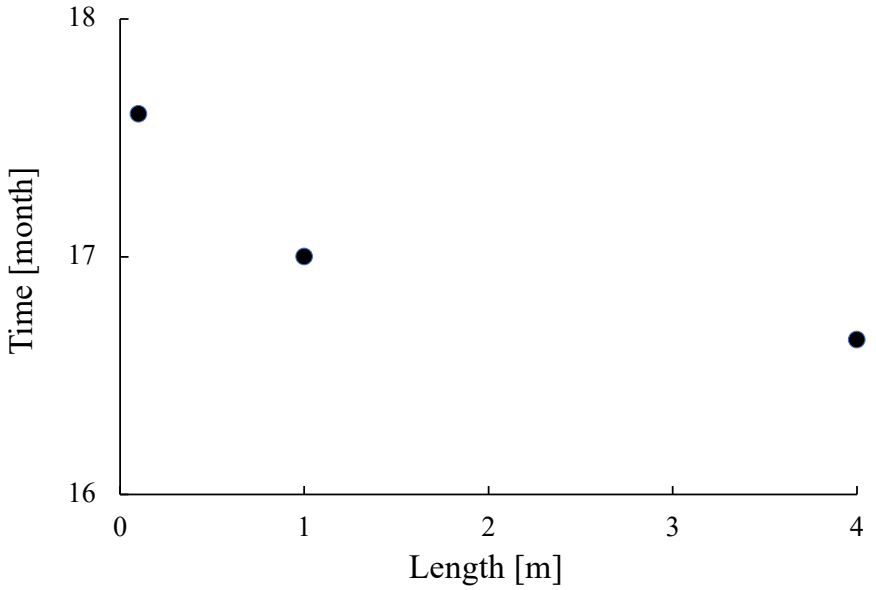

Figure 6.9: Length effect on the service lifetime of the cladding corresponding to $P_f = 10^{-6}$.

on the design lifetime, which needs to be taken into consideration in the design extrapolation. The direct consequence of this finding is that the safety factor determined based on the laboratory tests needs to be adjusted for the design of a full-length structure. Otherwise, the failure probability of the actual structure would be much larger than the tolerable value.

Chapter 7

Conclusion and Recommendations

7.1 Conclusions

- A robust multiaxial testing system is developed for generating various load combinations of axial force and internal pressure. To provide effective isolation (jacketing) from the internal fluid pressure, Viton membranes of a special shape are manufactured to seal both the internal surface of the specimen and the interface between the specimen and apparatus. High-strength epoxy is used in between the contracted surface of the specimen and apparatus to transmit axial loading. With this design, the system is able to load the specimen up to ultimate failure.

- A multiaxial failure model is proposed for SiC/SiC composites. The failure model is extended to capture the probabilistic behavior. It is shown that,

for the stress states of present interest, the probabilistic behavior of the failure surface can be well described for the probability distributions of the proportional limit stresses (PLS) in the axial, hoop, and biaxial directions.

- A new strain-based criterion is proposed for determining the PLS for multiaxial loading. The criterion reduces to the current ASTM recommendation on the PLS for uniaxial tensile loading. The proposed criterion is validated by the comparison with the results of acoustic emission. With the newly designed test apparatus, the multiaxial failure surface corresponding to the PLS with its statistical variation is experimentally measured.

- The time dependence of the failure statistics of SiC/SiC composites is formulated through a damage kinetics model. The damage accumulation mechanism indicates that the failure probability of the material at any given time is governed by the entire previous loading history, a key difference from the time-independent model in which the failure probability depends only on the current stress state.

- It is demonstrated that the damage growth kinetics has a profound influence on the time evolution of failure probability of the cladding. Therefore, to accurately predict the lifetime distribution of the cladding, it is crucial to calibrate the damage growth model for SiC/SiC composites. Based on the present model, it is suggested to use a combination of strength test and static fatigue lifetime test to calibrate the damage kinetics model.

- The failure probability of the SiC/SiC cladding is calculated from the material failure probability through a weakest-link model, which signifies the

damage localization mechanism. Since the cladding experiences a relatively uniform stress distribution along its height, the failure probability is strongly dependent on the cladding length. It shown that a longer cladding would experience a considerably higher failure probability as compared to a shorter one.

7.2 Recommendations

In this study, we define the failure of the entire structure to occur once any material element reaches the PLS. This definition is conservative because, in actual application, the cracks initiated at the cladding inner region could be arrested by the compressive stress at the outer region. In this case, the hermeticity of the system may be retained and the actual failure risk of the cladding would be lower than that calculated by the present model. To capture the behavior of crack propagation for estimating the failure risk, one would need to rely on stochastic numerical simulations (e.g. finite element analysis), which involve a nonlinear constitutive material model with spatially distributed random material properties (e.g. [75]). Such types of numerical models are appealing as they will yield a more accurate estimation of failure risk as well as reveal the cracking pattern at failure. Though the computational cost could be high, full-scale nonlinear stochastic computation will be feasible with the advances in modern computing technology. In comparison, the present model provides an efficient means for estimating an upper bound of failure risk while taking into account the effect of damage accumulation.

The finding of the present study indicates the importance of understanding the

subcritical damage growth behavior. In nuclear applications, the subcritical damage growth not only deteriorates the load-carrying capacity of the structure but also affects the structural integrity. So far most laboratory experiments focused solely on strength properties. There is a clear need to experimentally investigate the subcritical damage growth under sustained loading combined with other environmental conditions such as high temperatures and irradiation. Such experimental data will allow us to quantify the kinetics of subcritical damage growth, reveal the underlying mechanisms, and calibrate the relevant numerical and theoretical models.

The present model reveals the important consequences of the damage accumulation mechanism as well as the size effect for assessing the lifetime distribution of SiC/SiC composite cladding. These findings suggest the critical need for future work on experimental characterization of the mechanical behavior of SiC/SiC composite materials as an essential step toward the reliability-based design of SiC/SiC composite claddings.

References

[1] J. Lamon. *Chemical Vapor Infiltrated SiC/SiC Composites (CVI SiC/SiC)*, pages 55–76. Springer US, Boston, MA, 2005.

[2] T. Koyanagi, Y. Katoh, G. Singh, and M. Snead. SiC/SiC cladding materials properties handbook. *ORNL*, page 385, 2017.

[3] G. Singh, S. Gonczy, C. Deck, E. Lara-Curzio, and Y. Katoh. Interlaboratory round robin study on axial tensile properties of SiC-SiC CMC tubular test specimens. *International Journal of Applied Ceramic Technology*, 15(6):1334–1349, 2018, https://ceramics.onlinelibrary.wiley.com/doi/pdf/10.1111/ijac.13010.

[4] G. Singh, K. Terrani, and Y. Katoh. Thermo-mechanical assessment of full SiC/SiC composite cladding for LWR applications with sensitivity analysis. *Journal of Nuclear Materials*, 499:126 – 143, 2018.

[5] K. A. Terrani. Accident tolerant fuel cladding development: Promise, status, and challenges. *Journal of Nuclear Materials*, 501:13–30, 2018.

[6] Y. Katoh, K. Ozawa, C. Shih, T. Nozawa, R. J. Shinavski, A. Hasegawa, and L. L. Snead. Continuous SiC fiber, CVI SiC matrix composites for nuclear applications: Properties and irradiation effects. *Journal of Nuclear Materials*, 448(1-3):448–476, May 2014.

[7] K. A. Terrani, B. A. Pint, C. M. Parish, C. M. Silva, L. L. Snead, and Y. Katoh. Silicon carbide oxidation in steam up to 2 MPa. *Journal of the American Ceramic Society*, 97(8):2331–2352, 2014.

[8] F. Bernachy-Barbe, L. Gélébart, M. Bornert, J. Crépin, and C. Sauder. Anisotropic damage behavior of SiC/SiC composite tubes: Multiaxial testing and damage characterization. *Composites Part A: Applied Science and Manufacturing*, 76:281 – 288, 2015.

[9] C. P. Deck, G. M. Jacobsen, J. Sheeder, O. Gutierrez, J. Zhang, J. Stone, H. E. Khalifa, and C. A. Back. Characterization of SiC–SiC composites for accident tolerant fuel cladding. *Journal of Nuclear Materials*, 466:667 – 681, 2015.

[10] E. Rohmer, E. Martin, and C. Lorrette. Mechanical properties of SiC/SiC braided tubes for fuel cladding. *Journal of Nuclear Materials*, 453(1):16 – 21, 2014.

[11] K. Shapovalov, G. M. Jacobsen, L. Alva, N. Truesdale, C. P. Deck, and X. Huang. Strength of SiC_f-SiC_m composite tube under uniaxial and multi-axial loading. *Journal of Nuclear Materials*, 500:280 – 294, 2018.

[12] D. Kim, H.-G. Lee, J. Y. Park, and W.-J. Kim. Fabrication and measurement of hoop strength of SiC triplex tube for nuclear fuel cladding applications. *Journal of Nuclear Materials*, 458:29 – 36, 2015.

[13] L. Saucedo-Mora, T. Lowe, S. Zhao, P. D. Lee, P. M. Mummery, and T. J. Marrow. In situ observation of mechanical damage within a SiC-SiC ceramic matrix composite. *Journal of Nuclear Materials*, 481:13–23, 2016.

[14] T. Nozawa, S. Kim, K. Ozawa, and H. Tanigawa. Stress envelope of silicon carbide composites at elevated temperatures. *Fusion Engineering and Design*, 89(7):1723–1727, 2014.

[15] A. Haldar and S. Mahadevan. *Probability, Reliability, and Statistical Methods in Engineering Design*. Wiley, New York, 2000.

[16] J.-L. Le. Size effect on reliability indices and safety factors of quasibrittle structures. *Structural Safety*, 52:20–28, 2015.

[17] Z. P. Bažant and J.-L. Le. *Probabilistic Mechanics of Quasibrittle Structures: Strength, Lifetime, and Size Effect*. Cambridge University Press, 2017.

[18] J. G. Stone, R. Schleicher, C. P. Deck, G. M. Jacobsen, H. E. Khalifa, and C. A. Back. Stress analysis and probabilistic assessment of multi-layer SiC-based accident tolerant nuclear fuel cladding. *Journal of Nuclear Materials*, 466:682–697, 2015.

[19] Y. Deng, K. Shirvan, Y. Wu, and G. Su. Probabilistic view of SiC/SiC composite cladding failure based on full core thermo-mechanical response. *Journal of Nuclear Materials*, 507:24–37, 2018.

[20] W. Weibull. The phenomenon of rupture in solids. *Proc. Royal Sweden Inst. Engrg. Res.*, 153:1–55, 1939.

[21] W. Weibull. A statistical distribution function of wide applicability. *Journal of Applied Mechanics*, 153(18):293–297, 1951.

[22] E. Vanmarcke. *Random Fields Analysis and Synthesis*. World Scientific Publishers, Singapore, 2010.

[23] Z. P. Bažant and S.-D. Pang. Activation energy based extreme value statistics and size effect in brittle and quasibrittle fracture. *Journal of the Mechanics and Physics of Solids*, 55(1):91–131, 2007.

[24] Z. P. Bažant, J.-L. Le, and M. Z. Bazant. Scaling of strength and lifetime distributions of quasibrittle structures based on atomistic fracture mechanics. *Proceedings of the National Academy of Sciences*, 106:11484–11489, 2009.

[25] J.-L. Le, Z. P. Bažant, and M. Z. Bazant. Unified nano-mechanics based probabilistic theory of quasibrittle and brittle structures: I. strength, static crack growth, lifetime and scaling. *Journal of the Mechanics and Physics of Solids*, 59(7):1291–1321, 2011.

[26] M. Ben-Belgacem, V. Richet, K. A. Terrani, Y. Katoh, and L. L. Snead. Thermo-mechanical analysis of LWR SiC/SiC composite cladding. *Journal of Nuclear Materials*, 447(1):125 – 142, 2014.

[27] H. Moissan. Nouvelles recherches sur la météorité de cañon diablo. *Comptes rendus*, 139:773–86, 1904.

[28] E. G. Acheson. Production of artificial crystalline carbonaceous materials. *US492767*, 1983.

[29] Y. Katoh and L. L. Snead. Silicon carbide and its composites for nuclear applications–historical overview. *Journal of Nuclear Materials*, 526:151849, 2019.

[30] J. A. Lely. Sublimation process for manufacturing silicon carbide crystals. *US2854364A*, 1955.

[31] S. E. Saddow and A. K. Agarwal. *Advances in silicon carbide processing and applications*. Artech House, 2004.

[32] J. T. Kendall and D. Yeo. Preparation of pure silicon carbide. *Proc. Int. Congr. Pure Appl. Chem.*, 1947.

[33] H. J. Round. A note on carborundum. *Electr. World*, 49 (1907) 309.

[34] S. Yajima, K. Okamura, J. Hayashi, and M. Omori. Synthesis of continuous SiC fibers with high tensile strength. *Journal of the American Ceramic Society*, 59(7-8):324–327, 1976.

[35] R. R. Naslain. Sic-matrix composites: nonbrittle ceramics for thermostructural application. *International Journal of Applied Ceramic Technology*, 2(2):75–84, 2005.

[36] H. Liu, J.-H. Yang, Y.-R. Zhou, X.-X. Lyu, Z. Qi, and J. Jiao. Progress in coupon tests of SiC_f/SiC ceramic matrix composites used for aero engines. *Cailiao Gongcheng/Journal of Materials Engineering*, 46:1–12, 11 2018.

[37] G. S. Corman, A. J. Dean, S. Brabetz, M. K. Brun, K. L. Luthra, L. Tognarelli, and M. Pecchioli. Rig and engine testing of melt infiltrated ceramic composites for combustor and shroud applications. *J. Eng. Gas Turbines Power*, 124(3):459–464, 2002.

[38] N. P. Bansal and J. Lamon. *Ceramic matrix composites: materials, modeling and technology*. John Wiley & Sons, 2014.

[39] S. Yajima, J. Hayashi, M. Omori, and K. Okamura. Development of a silicon carbide fibre with high tensile strength. *Nature*, 261(5562):683–685, 1976.

[40] S. Yajima, J. Hayashi, and M. Omori. Continuous silicon carbide fiber of high tensile strength. *Chemistry Letters*, 4(9):931–934, 1975.

[41] C. K. Whitmarsh and L. V. Interrante. Synthesis and structure of a highly branched polycarbosilane derived from (chloromethyl) trichlorosilane. *Organometallics*, 10(5):1336–1344, 1991.

[42] T. Hinoki, E. Lara-Curzio, and L. L. Snead. Mechanical properties of high purity sic fiber-reinforced cvi-sic matrix composites. *Fusion science and technology*, 44(1):211–218, 2003.

[43] D. Justine, S. Eduardo, and A. N. Nasrin. Fracture behaviour of SiC/SiC ceramic matrix composite at room temperature. *Journal of the European Ceramic Society*, 42(7):3156–3167, 2022.

[44] L. L. Snead, S. J. Zinkle, and D. Steiner. Radiation induced microstructure and mechanical property evolution of sic/c/sic composite materials. *Journal of nuclear materials*, 191:560–565, 1992.

[45] L. L. Snead, D. Steiner, and S. J. Zinkle. Measurement of the effect of radiation damage to ceramic composite interfacial strength. *Journal of nuclear materials*, 191:566–570, 1992.

[46] G. W. Hollenberg, C. H. Henager Jr, G. E. Youngblood, D. J. Trimble, S. A. Simonson, G. A. Newsome, and E. Lewis. The effect of irradiation on the stability and properties of monolithic silicon carbide and SiC_f/SiC composites up to 25 dpa. *Journal of Nuclear Materials*, 219:70–86, 1995.

[47] L. L. Snead, M. C. Osborne, R. A. Lowden, J. Strizak, R. J. Shinavski, K. L. More, W. S. Eatherly, J. Bailey, and A. M. Williams. Low dose irradiation performance of sic interphase SiC/SiC composites. *Journal of nuclear materials*, 253(1-3):20–30, 1998.

[48] A. R. Bunsell and M.-H. Berger. Fine diameter ceramic fibres. *Journal of the European Ceramic Society*, 20(13):2249–2260, 2000.

[49] T. Koyanagi, Y. Katoh, T. Nozawa, L. L. Snead, S. Kondo, C. H. Henager Jr, M. Ferraris, T. Hinoki, and Q. Huang. Recent progress in the development of SiC composites for nuclear fusion applications. *Journal of Nuclear Materials*, 511:544–555, 2018.

[50] W. Yang, H. Araki, A. Kohyama, S. Thaveethavorn, H. Suzuki, and T. Noda. Fabrication in-situ SiC nanowires/SiC matrix composite by chemical vapor infiltration process. *Materials Letters*, 58(25):3145–3148, 2004.

[51] C. A. Nannetti, A. Ortona, D. A. de Pinto, and B. Riccardi. Manufacturing SiC-fiber-reinforced SiC matrix composites by improved CVI/slurry infiltration/polymer impregnation and pyrolysis. *Journal of the American Ceramic Society*, 87(7):1205–1209, 2004.

[52] L. L. Snead, Y. Katoh, A. Kohyama, J. L. Bailey, N. L. Vaughn, and R. A. Lowden. Evaluation of neutron irradiated near-stoichiometric silicon carbide fiber composites. *Journal of Nuclear Materials*, 283:551–555, 2000.

[53] J. B. J. Hegeman, J. G. Van der Laan, M. Van Kranenburg, M. Jong, D. d'Hulst, and P. Ten Pierick. Mechanical and thermal properties of SiC_f-SiC_m composites irradiated with neutrons at high temperatures. *Fusion engineering and design*, 75:789–793, 2005.

[54] K. Ozawa, T. Nozawa, Y. Katoh, T. Hinoki, and A. Kohyama. Mechanical properties of advanced SiC/SiC composites after neutron irradiation. *Journal of nuclear materials*, 367:713–718, 2007.

[55] G. Bertolino, G. Meyer, and J. P. Ipina. Degradation of the mechanical properties of zircaloy-4 due to hydrogen embrittlement. *Journal of alloys and compounds*, 330:408–413, 2002.

[56] D. M. Carpenter. *An assessment of silicon carbide as a cladding material for light water reactors*. PhD thesis, Massachusetts Institute of Technology, 2010.

[57] T. Koyanagi, Y. Katoh, and T. Nozawa. Design and strategy for next-generation silicon carbide composites for nuclear energy. *Journal of Nuclear Materials*, 540:152375, 2020.

[58] T. Koyanagi, Y. Katoh, K. Ozawa, K. Shimoda, T. Hinoki, and L. L. Snead. Neutron-irradiation creep of silicon carbide materials beyond the initial transient. *Journal of Nuclear Materials*, 478:97–111, 2016.

[59] H. M. Yun and J. A. DiCarlo. Comparison of the tensile, creep, and rupture strength properties of stoichiometric SiC fibers. In *23rd Annual Conference on Composites, Advanced Ceramics, Materials, and Structures: A: Ceramic Engineering and Science Proceedings*, pages 259–272. Wiley Online Library, 1999.

[60] A. Urano, J.-I. Sakamoto, M. Takeda, Y. Imai, H. Araki, and T. Noda. Microstructure and mechanical properties of SiC fiber "Hi-Nicalon Type S" reinforced SiC composites. In *22nd Annual Conference on Composites, Advanced Ceramics, Materials, and Structures: A: Ceramic Engineering and Science Proceedings*, volume 19, pages 55–63. Wiley Online Library, 1988.

[61] M. Takeda, J. Sakamoto, A. Saeki, and H. Ichikawa. Mechanical and structural analysis of silicon carbide fiber Hi-Nicalon type S. In *Proceedings of the 20th Annual Conference on Composites, Advanced Ceramics, Materials, and Structures—B: Ceramic Engineering and Science Proceedings*, pages 35–42. Wiley Online Library, 1996.

[62] H. Ichikawa. Polymer-derived ceramic fibers. *Annual Review of Materials Research*, 46:335–356, 2016.

[63] C. P. Deck, H. E. Khalifa, B. Sammuli, T. Hilsabeck, and C. A. Back. Fabrication of SiC–SiC composites for fuel cladding in advanced reactor designs. *Progress in Nuclear Energy*, 57:38–45, 2012.

[64] ASTM International. ASTM C1773-21: Standard Test Method for Monotonic Axial Tensile Behavior of Continuous Fiber-Reinforced Advanced Ceramic Tubular Test Specimens at Ambient Temperature. West Conshohocken, PA, 2021.

[65] ASTM International. ASTM C1819-21: Standard Test Method for Hoop Tensile Strength of Continuous Fiber-Reinforced Advanced Ceramic Composite Tubular Test Specimens at Ambient Temperature Using Elastomeric Inserts. West Conshohocken, PA, 2021.

[66] J.-L. Le and Z. P. Bažant. Strength distribution of dental restorative ceramics: Finite weakest link model with zero threshold. *Dental Materials*, 25(5):641–648, 2009.

[67] C. Hu, J. F. Labuz, T. Koyanagi, and J.-L. Le. Mechanistic modeling of lifetime distribution of SiC/SiC composite claddings. *Journal of the American Ceramic Society*, 106(5):3066–3077, 2023.

[68] Y. N. Rabotnov. *Creep Problem in Structural Members*. North-Holland, Amsterdam, 1969.

[69] L. Kachanov. *Introduction to continuum damage mechanics*. Springer Netherlands, Dordrecht, 1986.

[70] M. Kachanov. On the concept of damage in creep and in the brittle-elastic range. *Int J Damage Mech*, 3:329–337, 10 1994.

[71] R. A. Fisher and L. H. C. Tippett. Limiting forms of the frequency distribution of the largest or smallest member of a sample. In *Mathematical Proceedings of the Cambridge Philosophical Society*, volume 24, pages 180–190. Cambridge University Press, 1928.

[72] A. M. Freudenthal. Statistical approach to brittle fracture, chapter 6. *FRACTURE, An Advanced Tratise Volume II, Mathematical Fundamentals*, 1968.

[73] Z. P. Bazant and J. Planas. *Fracture and size effect in concrete and other quasi-brittle materials*, volume 16. CRC press, 1997.

[74] Z. P. Bazant and G. Lewis. Scaling of structural strength. *Appl. Mech. Rev.*, 56(5):B70–B72, 2003.

[75] A. Gorgogianni, J. Eliáš, and J.-L. Le. Mesh objective stochastic simulations of quasi-brittle fracture. *Journal of the Mechanics and Physics of Solids*, 159:104745, 2022.

Appendix A

Strength Parameters for Individual Tests

Specimen	**AE PLS [MPa]**	**Strain PLS [MPa]**	**UTS [MPa]**
1	80.5	109.1	193.3
2	97.8	108.1	194.5
3	86.2	115.5	212.7
4	80.5	105.4	211.8
5	102.6	112.1	201.8
6	82.3	94.5	198.4
7	96.5	92	197.7
8	91	95.6	209.7
9	81.2	97.9	190.1
10	101.1	112.4	225.3
Average	90.0	104.3	203.5
Std	8.5	8.1	10.5
Cov	9.4%	7.8%	5.1%

Table A.1: Strength parameters for uniaxial tension tests.

Specimen	**AE PLS [MPa]**	**Strain PLS [MPa]**	**UTS [MPa]**
1	78.8	92.4	173.4
2	81.6	105.4	169.3
3	74.6	101.1	187.6
4	85.6	102.9	178.9
5	73.7	97.3	170.9
6	62.9	113.3	163.5
7	79.0	85.2	167.2
8	89.4	115.6	167.6
9	76.2	110.7	173.0
10	83.1	101.9	217.9
Average	78.5	102.6	176.9
Std	7.0	8.9	15.1
Cov	8.9%	8.7%	8.5%

Table A.2: Strength parameters for hoop tension tests.

Specimen	**AE PLS [MPa]**	**Strain PLS [MPa]**	**UTS [MPa]**
1	91.9	123.6	204.7
2	106.4	124.4	196.1
3	90.2	98.7	189.5
4	80.1	115.0	226.3
5	103.5	105.8	195.3
6	85.1	93.7	199.7
7	79.6	130.4	209.4
8	108.7	90.0	215.8
9	84.0	136.2	198.4
10	95.3	119.6	207.7
Average	92.5	113.7	204.3
Std	10.2	15.1	10.4
Cov	11.0%	13.3%	5.1%

Table A.3: Strength parameters for biaxial tension tests.

Specimen	**AE PLS [MPa]**	**Strain PLS [MPa]**	**UTS [MPa]**
1	121.1	119.4	223.6
2	96.8	120.0	265.8
3	89.1	138.3	278.1
4	102.3	102.9	279.1
5	89.5	122.9	278.5
6	119.7	117.7	313.4
7	106.4	125.0	255.1
8	102.4	117.6	260.3
9	96.9	124.6	246.0
10	107.4	141.5	258.2
Average	103.2	123.0	265.8
Std	10.4	10.3	22.7
Cov	10.1%	8.4%	8.5%

Table A.4: Strength parameters for loading path $\sigma_{zz}/\sigma_{\theta\theta} = 2$.

Specimen	**AE PLS [MPa]**	**Strain PLS [MPa]**	**UTS [MPa]**
1	92.6	138.9	193.9
2	88.8	127.5	234.5
3	77.9	145.8	188.1
4	82.2	113.4	190.1
5	73.8	142.5	178.9
6	74.5	102.2	174.6
7	83.5	139.6	175.5
8	88.0	105.0	186.5
9	72.1	142.8	202.0
10	74.3	153.1	243.6
Average	80.8	131.1	196.8
Std	6.9	17.2	22.7
Cov	8.6%	13.1%	11.5%

Table A.5: Strength parameters for loading path $\sigma_{zz}/\sigma_{\theta\theta} = 0.5$.